Physics of Fluids

On the scattering of focused wave by a finite surface-piercing circular cylinder: A numerical investigation

Cite as: Phys. Fluids **34**, 035132 (2022); https://doi.org/10.1063/5.0086826
Submitted: 29 January 2022 • Accepted: 07 March 2022 • Published Online: 21 March 2022

Songtao Chen (陈松涛), Weiwen Zhao (赵伟文) and Decheng Wan (万德成)

COLLECTIONS

This paper was selected as an Editor's Pick

View Online Export Citation CrossMark

ARTICLES YOU MAY BE INTERESTED IN

Eulerian and Lagrangian transport by shallow-water breaking waves
Physics of Fluids **34**, 032116 (2022); https://doi.org/10.1063/5.0086434

Turbulence structure in a very sharp thermally stratified open-channel meander
Physics of Fluids **34**, 035130 (2022); https://doi.org/10.1063/5.0083230

Effect of the odd and even number of blades on the hydrodynamic performance of a pre-swirl pumpjet propulsor
Physics of Fluids **34**, 035120 (2022); https://doi.org/10.1063/5.0080661

AIP Publishing

© 2022 Author(s).

Physics of Fluids ARTICLE scitation.org/journal/phf

On the scattering of focused wave by a finite surface-piercing circular cylinder: A numerical investigation

Cite as: Phys. Fluids **34**, 035132 (2022); doi: 10.1063/5.0086826
Submitted: 29 January 2022 · Accepted: 7 March 2022 ·
Published Online: 21 March 2022

View Online Export Citation CrossMark

Songtao Chen (陈松涛), Weiwen Zhao (赵伟文), and Decheng Wan (万德成)[a]

AFFILIATIONS

Computational Marine Hydrodynamics Lab (CMHL), School of Naval Architecture, Ocean and Civil Engineering, Shanghai Jiao Tong University, Shanghai 200240, China

[a]Author to whom correspondence should be addressed: dcwan@sjtu.edu.cn

ABSTRACT

For nonlinear wave–structure interactions, the high-frequency scattered waves can be identified within the drag-inertia regime, especially in steep incident waves where viscous effects are not negligible. According to previous studies, this unexpected phenomenon is highly associated with the local flow field, posing challenges to the existing harmonic-based diffraction solutions (mostly up to second-order). To overcome these shortcomings in potential flows, we establish a high-fidelity numerical wave tank to solve this two-phase free surface flow in the open source computational fluid dynamics framework OpenFOAM. We implement the ghost fluid method to eliminate the spurious velocities, mostly reported in two-phase volume of fluid solvers, in the vicinity of the free surface and preserve a sharp air–water interface. A modified generating–absorbing boundary condition is employed to achieve high computational efficiency without passive relaxation zones. Good agreement with experimental data demonstrates the reliability and accuracy of the present numerical wave tank in extreme wave conditions. On this basis, this paper numerically investigates the wave scattering of the focused wave by a finite surface-piercing circular cylinder, with emphasis on the flow mechanism. Three types of high-frequency scattered waves are identified in the near field, namely, *Type*-1, *Type*-2, and *Type*-1* waves. The typical mechanisms of each type are analyzed in depth with detailed flow field data, which confirms and complements the observations from previous experiments. More importantly, the primary vortical structures involved in scattering are extracted by the Liutex vortex identification method. The behaviors of these vortical structures could characterize the evolution of the high-frequency scattered waves and provide new insights into this strongly nonlinear phenomenon. An overall schematic of the wave scattering evolution in this complex condition is summarized for a straightforward understanding.

Published under an exclusive license by AIP Publishing. https://doi.org/10.1063/5.0086826

I. INTRODUCTION

The interaction between the wave and a surface-piercing cylinder has received sustained attention for decades due to its practical significance in the design and production of offshore platforms. As a highly nonlinear phenomenon involved, wave scattering is found to be important in certain flow regimes, dependent upon the diameter D and the incident wavelength λ. When the cylinder is large, i.e., $D/\lambda > 0.2$, the structure is considered to cause evident disturbances to the incident wave field. Therefore, a number of linear or high-order diffraction solutions based upon the harmonic analysis have been established to take into account the scattered field. When the cylinder is small, i.e., $D/\lambda < 0.2$, the disturbances are generally considered minor and thus can be ignored. However, according to the systematic experimental studies by Swan *et al.*,[1–3] this classification is not strictly for the steep incident conditions where viscous effects possibly play important roles, e.g., flow separation and vortex shedding. When the flow falls within the regime $D/\lambda < 0.2$, two undocumented high-frequency scattered waves can be identified in both steep regular and focused waves, namely, *Type*-1 and *Type*-2, as shown in Fig. 1. Since the evolution of these scattered waves is highly related to the local flow around the cylinder, the existing diffraction solutions based on the Taylor expansion (mostly up to second-order) cannot account for these high-frequency components. As a result, it usually leads to a large discrepancy in wave loading predictions. On the other hand, it is difficult for numerical methods based on potential flow theory to reproduce this highly nonlinear phenomenon for further analysis, especially in steep waves.[4,5]

Published under an exclusive license by AIP Publishing

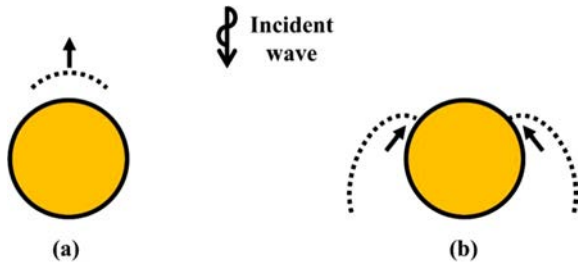

FIG. 1. Illustration of high-frequency wave scattering in regular waves: (a) *Type*-1 and (b) *Type*-2.

Experimental observation is considered the most straightforward method for a preliminary exploration. By analyzing the records of wave gauges and the high-quality photos by high-speed digital cameras, Swan *et al.* concluded that the *Type*-1 wave is attributed to the run-up and wash-down near the stagnation points, and the *Type*-2 wave is associated with the circulation of fluid around the cylinder. However, due to the limitation of observation methods, it is hard to obtain detailed information about the flow field for an in-depth understanding. Therefore, it is necessary to introduce a powerful numerical tool for further analysis.

With the rapid development of high-performance computers, computational fluid dynamics (CFD) offers the capability of solving fully nonlinear governing equations, which can well capture these high-frequency scattered waves. A large number of numerical simulations have reported their existence in different wave conditions. Chen *et al.*[6] used OpenFOAM to simulate the wave–structure interaction of a bottom-mounted vertical circular cylinder; they observed similar scattered waves in the case of a focused wave group with $kA = 0.2$ (where k is the wavenumber and A is the crest amplitude). Similarly, Chen *et al.*[7] developed a 3D parallel particle-in-cell solver to simulate the same working condition and additionally confirmed the existence of high-frequency scattered waves in the case of regular waves with $kA = 0.2$. Mohseni *et al.*[8] adopted the IHFOAM toolbox to establish a numerical wave tank and simulated the ITTC benchmark tests of a truncated circular cylinder in regular waves; they mainly analyzed the relationships with wavelength and wave steepness in terms of the harmonics of run-up heights and the high-frequency scattered waves.

Nevertheless, previous numerical studies have paid little or no attention to the formation mechanism of these high-frequency scattered waves. Most of them still focused on common overall quantities, such as wave elevation and wave loading, which did not fully utilize the advantages of CFD in resolving the entire flow field. For these reasons, it is of great importance to analyze the scattered waves from the perspective of the local flow field, but before that, how to handle the spurious air velocities above the free surface in the numerical simulations, mostly reported in two-phase volume of fluid (VOF) solvers, becomes a significant problem. Afshar[9] reported the severe spurious air velocities in wave generation of an OpenFOAM-based numerical wave tank, especially the horizontal component. The reason for this unphysical problem is that the original VOF method of the weighted average concept cannot deal with the jump conditions in large density ratio two-phase flows; his work found that the possible shortcomings are the unexpected wave breaking and the unwanted phase-lag between numerical and analytical solutions. These numerical problems will undoubtedly affect the accuracy of the local velocity field and may lead to misunderstandings of the flow mechanism.

To eliminate the spurious air velocities in air–water two-phase flows, the ghost fluid method (GFM) has been proven to be an effective approach. By constructing the corresponding ghost nodes/cells on the other side of the real fluid, the GFM can handle the discontinuous variables across the interface, e.g., pressure, density, and viscosity, thus achieving the required jump conditions. The GFM was first proposed by Fedkiw *et al.*[10] for two-phase compressible flows on a Cartesian grid and later was extended by Kang *et al.*[11] for viscous incompressible air–water flows. In marine hydrodynamics, the GFM has also shown its superior capabilities in a wide range of applications. Huang *et al.*[12] implemented the GFM with the two-phase level-set method on curvilinear body-fitted grids and applied it to the flow around a surface combatant model; the comparisons with experimental measurements showed its good performance in free surface flows. Queutey and Visonneau[13] extended the GFM to unstructured grids with the VOF method; in the flow around the Series 60 ship model, excellent agreement was achieved in terms of free surface elevation and velocity field. Vukčević *et al.*[14] first implemented the GFM in the arbitrary polyhedral framework of OpenFOAM for large-scale air–water flows and gave a thorough description of numerical discretization; in their implementation, the surface tension was neglected, and the viscosity was still assumed continuous across the interface. On this basis, Peltonen *et al.*[15,16] took a special treatment for the viscous term and proved its improvement with a benchmark shear flow. Based on these previous developments, the GFM has gradually been applied to wave simulations. Vukčević *et al.*[17,18] and Li[19] adopted the GFM in their coupled viscous/potential models to simulate the 2D wave propagations and the wave diffraction of a 3D vertical circular cylinder in regular waves. Liu *et al.*[20] used the GFM to eliminate the spurious air velocities in wave-breaking simulations and thus assessed the performances of different turbulent models; their simulations confirmed that the spurious velocities result in an earlier breaking position.

In summary, the numerical simulations using the GFM can obtain a more physical flow field and thus provide insights into the formation of the high-frequency scattered waves. However, to the author's knowledge, few scholars have thoroughly studied their behaviors and mechanisms, especially in complex extreme wave conditions. For example, Kasiman[21] used OpenFOAM to reproduce the experiments by Swan *et al.*, but still preferred to explain the physics from surface elevation. To fill this gap regarding the flow mechanisms, a high-fidelity simulation is performed to study the high-frequency scattered waves of focused wave interactions with a finite surface-piercing circular cylinder. The primary objects are to (i) establish a high-fidelity numerical wave tank for focused wave simulations using the GFM and generating–absorbing boundary conditions (GABC); (ii) explain the mechanisms of high-frequency scattered waves from the local flow field; and (iii) summarize the evolution of wave scattering in focused wave conditions.

The remainder of this paper is organized as follows. First, the numerical methods used to establish the high-fidelity numerical wave tank are introduced in Sec. II, including the GFM, geometric VOF method, and GABC boundary conditions. Section III describes the numerical setups in detail. Among them, a mesh convergence study is carried out to determine the mesh configuration, and the adverse effects of spurious air velocities are also discussed. In Sec. IV, the mechanisms of the high-frequency scattered waves involved in this

Published under an exclusive license by AIP Publishing

complex flow are analyzed in terms of wave elevation, velocity field, and vortical structures. Finally, conclusions are drawn in Sec. V.

II. NUMERICAL METHODS

A. Governing equations

In the present study, all simulations are carried out by the open source finite volume CFD toolbox OpenFOAM v8. In the original two-phase incompressible VOF solver interFoam, the governing equations are as follows:

$$\nabla \cdot \mathbf{U} = 0, \tag{1}$$

$$\frac{\partial \rho \mathbf{U}}{\partial t} + \nabla \cdot (\rho \mathbf{U}\mathbf{U}) = -\nabla p_d - \mathbf{g} \cdot \mathbf{x} \nabla \rho + \nabla \cdot (\mu_{eff} \nabla \mathbf{U}) + f_\sigma, \tag{2}$$

where $\mathbf{U}$ is the velocity, ρ is the density, $\mathbf{g}$ is the acceleration of gravity, $\mathbf{x}$ is a Cartesian coordinate vector, $p_d = p - \rho \mathrm{g} \cdot \mathrm{x}$ is the dynamic pressure, μ_{eff} is the effective dynamic viscosity, and f_σ is the surface tension term. Here, the variable density ρ and viscosity μ are assumed continuous across the free surface using the phase fraction α_v,

$$\rho = (1 - \alpha_v)\rho_a + \alpha_v \rho_w, \tag{3}$$

$$\mu = (1 - \alpha_v)\mu_a + \alpha_v \mu_w. \tag{4}$$

On the RHS of Eq. (2), the co-existence of the dynamic pressure gradient term $-\nabla p_d$ and the density gradient term $-\mathrm{g} \cdot \mathrm{x} \nabla \rho$ brings troubles to the solution algorithm. Because most CFD codes employ segregated strategies, the phase fraction is solved with the velocity of the previous time step, and then the weighted density is obtained accordingly. However, the dynamic pressure is updated in each iteration of the present time step. On the other hand, the usual linear interpolation fails to meet the jump conditions and thus obtains the incorrect gradients of p_d and ρ, both of which vary dramatically across the free surface. Therefore, these numerical errors will cause an imbalance between $-\nabla p_d$ and $-\mathrm{g} \cdot \mathrm{x} \nabla \rho$, resulting in an unphysical non-zero source term on the RHS of Eq. (2). It can explain the generation of spurious velocities, which are more severe in the low-density air phase due to ρ as pre-factors on the LHS of Eq. (2).

To address this issue, we implemented the ghost fluid method (GFM) to meet free surface jump conditions, in which the density and the dynamic pressure are both assumed sharp across the free surface. The basic ideas and procedures are based on the previous work by Vukčević *et al.*[14] After considering free surface jump conditions, the momentum equation becomes

$$\frac{\partial \mathbf{U}}{\partial t} + \nabla \cdot (\mathbf{U}\mathbf{U}) = -\beta \nabla p_d + \nabla \cdot (\nu_{eff} \nabla \mathbf{U}), \tag{5}$$

where ν_{eff} is the effective kinematic viscosity, and β is either the inverse air density $1/\rho_a$ or the inverse water density $1/\rho_w$. Here, the viscosity is still assumed continuous, and the surface tension is neglected due to the large-scale characteristics in marine hydrodynamics. Note that the laminar model is used in this study because of the minor turbulence effect in non-breaking wave conditions, but the current implementation allows the application of various existing turbulence approaches, such as Reynolds-averaged Navier-Stokes (RANS) method, detached-eddy simulation (DES), and large eddy simulation (LES), without any additional changes.

Since the flows are considered incompressible with constant density in each phase, Eq. (5) is similar to the momentum equation of incompressible single-phase flows. The main difference is the special treatments for $-\beta \nabla p_d$ when the free surface lies between the adjacent cell centers P and N, i.e., $(\alpha_{vP} - 0.5)(\alpha_{vN} - 0.5) < 0$. Here, $\alpha_v = 0.5$ is regarded as the free surface in the VOF method. When the cells are away from the free surface, the inverse density β can be directly positioned inside the divergence operator. However, when the cells are near the free surface, the one-sided extrapolations have to be adopted for the dynamic pressure and density. For dynamic pressure, the corresponding ghost cell is constructed on the other side of the real fluid to calculate the gradient instead of the actual adjacent cell. Its value is correlated with the relative distance to the free surface $(\alpha_{vP} - 0.5)/(\alpha_{vP} - \alpha_{vN})$. For density, the value is simply determined by whether the cell is wet $(\alpha_v > 0.5)$ or dry $(\alpha_v < 0.5)$.

In fact, the above treatments are primarily for the discretization of the pressure Poisson equation,

$$\nabla \cdot \left(\frac{1}{a_p} \beta \nabla p_d \right) = \nabla \cdot \left(\frac{\mathbf{H}(\mathbf{U}_N)}{a_p} \right), \tag{6}$$

where a_p is the diagonal coefficient of the semi-discretized form of Eq. (5), and $\mathrm{H}(\mathrm{U}_N)$ consists of the source term and the contribution from all neighbor cells. In this regard, a modified Laplacian scheme is required for the diffusion term on the LHS. Moreover, due to explicit non-orthogonal correction, a modified gradient scheme is also necessary for the gradient term $\beta \nabla p_d$. For detailed information, refer to Ref. 14. In the Appendix, a standard test case for free surface flows is used to validate our implementation of the GFM and show its numerical improvements.

B. Interface capturing method

To accurately capture the interface, the volume of fluid (VOF) method[22] is adopted in our simulations. A scalar field α_v, which is defined as the volume fraction of the heavier phase (Here refers to water) in each cell, is used to locate the interface. The transport equation is given below:

$$\frac{\partial \alpha_v}{\partial t} + \nabla \cdot (\alpha_v \mathbf{U}) = 0. \tag{7}$$

Using Gauss's theorem, the discretized integral form of the advection term in Eq. (7) can be rewritten as

$$\int_V \nabla (\alpha_v \mathbf{U}) dV = \int_{\partial V} (\alpha_v \mathbf{U}) \cdot \mathbf{n} dS = \sum_f \alpha_{vf} \cdot \phi_f, \tag{8}$$

where $\mathbf{n}$ is the unit face normal, α_{vf} is the face interpolated volume fraction, and ϕ_f is the volume flux. To reduce the numerical diffusion, the challenge lies in how to get the precise interpolated value α_{vf} in advection. In addition to the original algebraic interface compression approach proposed by Weller,[23] OpenFOAM v8 also provides a geometric method based on the piecewise-linear interface calculation (PLIC). The primary idea is to split each cell with surface-cuts, the orientation of which is determined by the point interpolated value α_{vp}. According to the submerged area on each face, α_{vf} can then be calculated with the concept of geometric interface reconstruction. For those cells that cannot fully resolve the interface, the algebraic interface compression approach will still be applied, and thus α_{vf} will include the contribution from the artificial compression term. This flexible

Published under an exclusive license by AIP Publishing

strategy will significantly improve the solution's accuracy to get the sharp interface while enhancing the robustness for complex practical problems. Considering the above strengths, we adopt this PLIC-based geometric VOF method in the present study. A detailed description of the procedure was given in Ref. 24.

C. Wave generation and absorption

The third-party library waves2Foam developed by Jacobsen[25] is adopted for wave generation and absorption. In the present numerical wave tank, we employ a new generating–absorbing boundary condition (GABC) instead of the passive relaxation zone technique. This open boundary can achieve low reflection coefficients for dispersive waves without the relaxation (dissipation) zone, thus greatly saving the computational cost. Meanwhile, when the incident wave theories (including pressure and velocity) are known, this boundary condition can also generate required waves. For its detailed derivation and performance, refer to Ref. 26. Recently, a simplified variant has been implemented in wave2Foam by Borsboom and Jacobsen[27] and validated through a series of 2D wave propagation cases. However, since it was originally derived based on free surface continuous conditions, we have to make necessary modifications under the GFM framework. Here, a detailed description is presented:

This boundary condition is based on the classical Sommerfeld radiation condition, which only performs perfectly for waves with constant phase velocity c. For dispersive waves, a depth-varying function $c(z)$ is proposed to replace the constant value c,

$$\frac{\partial \Phi}{\partial t} + c(z)\frac{\partial \Phi}{\partial x} = 0, \tag{9}$$

where different forms of $c(z)$ were already given in Ref. 27. In order to convert the velocity potential Φ into variables in the Navier–Stokes equations, the linear Bernoulli equation is used,

$$p = -\rho_w g z - \rho_w \frac{\partial \Phi}{\partial t}, \tag{10}$$

where p is the total pressure and ρ_w is the water density. When inserting Eq. (10) into Eq. (9), the boundary condition then can be expressed with dynamic pressure p_d and velocity $\mathbf{U}$,

$$-(p_d)_b + \rho_w c(z)\mathbf{n}_b \cdot \mathbf{U}_b = S^G, \tag{11}$$

where $()_b$ represents the variables on the boundary face, and S^G is the source term for wave generation. To further eliminate the velocity U_b, the semi-discretized form of Eq. (5) is required,

$$\mathbf{U}_b = \frac{(\mathbf{H}(\mathbf{U}_N))_b}{(a_p)_b} - \left(\frac{1}{a_p}\right)_b (\beta)_{b_\Gamma} (\nabla p_d)_{b_\Gamma}, \tag{12}$$

where $()_\Gamma$ represents the special treatment near the interface, i.e., the above-mentioned one-sided extrapolation. Since this boundary condition is essentially imposed on the water column, we follow the same criterion in the GFM framework to determine the wet boundary face, i.e., $\alpha_f > 0.5$. Therefore, $(\beta)_{b_\Gamma}$ can be directly expressed as the inverse water density β_w. When Eq. (12) is substituted into Eq. (11), we can finally obtain the boundary condition for dynamic pressure p_d,

$$\left(1 + \frac{c(z)}{\Delta}\left(\frac{1}{a_p}\right)_b\right)(p_d)_b = \frac{c(z)}{\Delta}\left(\frac{1}{a_p}\right)_b (p_d)_C + \frac{c(z)}{\beta_w}\frac{(\mathbf{H}(\mathbf{U}_N))_b}{(a_p)_b} - S^G, \tag{13}$$

where Δ is the distance between the boundary face center and the adjacent cell center, and $()_C$ represents the variables of the owner cell of the boundary face. It is worth noting that the gradient term of dynamic pressure $(\nabla p_d)_{b_\Gamma}$ still uses the usual linear interpolation method, i.e., $(\nabla p_d)_{b_\Gamma} = \frac{(p_d)_b - (p_d)_C}{\Delta}$. This is because the free surface at the inlet/outlet is relatively flat with respect to the size of the mesh, which means the situation where the free surface lies between the boundary face center and the adjacent cell center almost does not exist.

D. Extreme wave model

To reproduce extreme wave conditions, the linear NewWave theory[28] is used to generate phase-focused waves at the target position and time. In this theory, a number of linear waves with specific phases are linearly superimposed. The wave elevation can then be expressed as

$$\eta(x,t) = \sum_{i=1}^{N} A_i \cos\left(k_i(x - x_c) - \omega_i(t - t_c)\right), \tag{14}$$

where x_c and t_c are the target position and time, respectively. Based on the specified wave spectrum, the amplitude A_i of each wave component is determined by

$$A_i = A_c \frac{S(f_i)\Delta f}{\sum_{i=1}^{N} S(f_i)\Delta f}, \tag{15}$$

where A_c is the target crest amplitude, $S(f_i)$ is the wave spectral density of the ith component with wave frequency f_i, and Δf is the frequency interval usually with a uniform distribution. The wave spectral density is computed with the JONSWAP wave spectrum[29] as follows:

$$S(f) = a\frac{H_s^2 f_p^4}{f^5}\exp\left[-\frac{5}{4}\left(\frac{f_p}{f}\right)^4\right]\gamma^b, \tag{16}$$

where H_s is the significant wave height, f_p is the peak wave frequency, and γ is the peak lifting factor. Here, γ is set to a default value of 3.3. a and b are defined as

$$a = \frac{0.0624}{0.23 + 0.0336\gamma - 0.185/(1.9 + \gamma)}, \tag{17}$$

$$b = \exp\left[\frac{-(f - f_p)^2}{2\sigma^2 f_p^2}\right], \tag{18}$$

$$\sigma = \begin{cases} 0.07, & f \le f_p, \\ 0.09, & f > f_p. \end{cases} \tag{19}$$

III. NUMERICAL SETUP

A. Computational model

According to the experiments in the COAST Laboratory Ocean Basin at Plymouth University, a finite surface-piercing cylinder is used to study the high-frequency scattered waves. The cylinder has a diameter D of 0.3 m and a height L of 0.3 m. The front of the cylinder is located at the focus position x_c, and the submerged depth H is 0.15 m at still water. In the experiment, the cylinder was fixed, and all degrees of freedom were restricted.

Published under an exclusive license by AIP Publishing

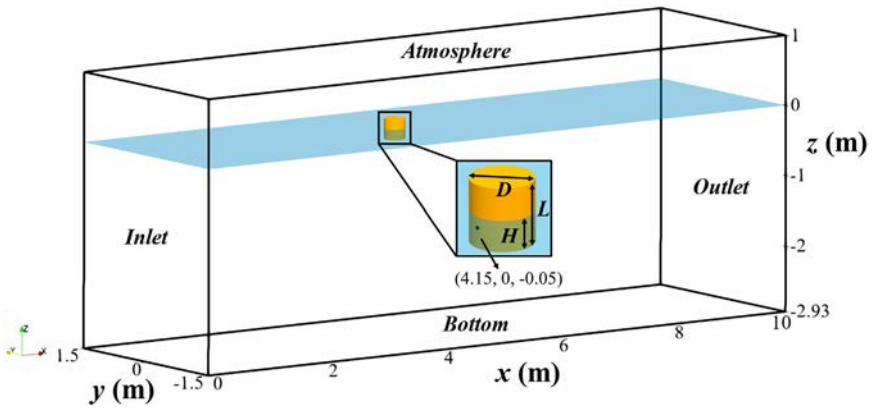

FIG. 2. Computational domain (where the local enlargement shows the geometric parameters of the cylinder and the position of a pressure probe).

In the present simulation, a rectangle computational domain is adopted for the numerical wave tank, as shown in Fig. 2. The origin of the coordinate system is at the intersection of the inlet with the longitudinal symmetry plane at still water. The water depth is set to 2.93 m, which equals to the working depth of the experimental basin. The application of GABC boundary conditions leads to a shorter domain length without the relaxation zone in the far field. As a result, the size of the computational domain is finally set to $0 \leq x \leq 10$ m, $-1.5 \leq y \leq 1.5$ m, and $-2.93 \leq z \leq 1$ m (length × width × depth).

To better explore the flow mechanism, a high-quality body-fitted structured mesh is adopted, as shown in Fig. 3. According to the convergence study discussed later, the mesh finally consists of 6.3×10^6 cells with refinement regions around the free surface. In the vicinity of the cylinder surface, several O-grid blocks are used to capture the topology to improve the quality near the free end. The height of the first near-wall layer is set to $5 \times 10^{-3} D$, and the expansion ratio is set to 1.05. At the same time, the mesh gradually becomes coarse toward the boundaries away from the free surface.

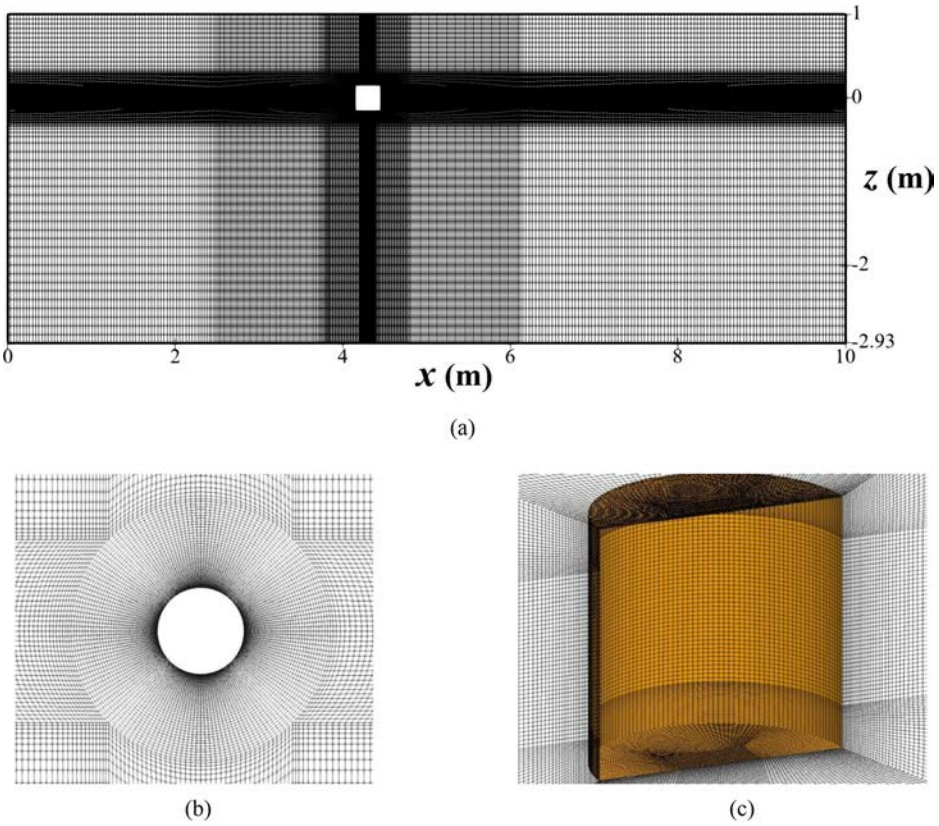

FIG. 3. Computational mesh: (a) overview on x-z plane ($y = 0$), (b) magnified view on x-y plane ($z = 0$), and (c) magnified view near free end.

Published under an exclusive license by AIP Publishing

B. Boundary conditions and numerical schemes

For wave generation and absorption, the GABC boundary condition is applied to the inlet and outlet. The bottom and cylinder are both treated as no-slip walls, while the Neumann boundary condition is imposed on the atmosphere. As for the lateral sides, the symmetry boundary condition is used.

To reduce the numerical dissipation during the wave propagation, a blended scheme between the first-order Euler scheme and the second-order Crank–Nicolson scheme is used for the temporal discretization. According to a sensitive study of Zhuang and Wan,[30] the blending factor is set to 0.95 as recommended. For the spatial discretization, the advection term and the diffusion term in the momentum equation are discretized using a second-order limitedLinearV scheme[31] and a second-order linear scheme, respectively. Note that the diffusion term in the pressure Poisson equation is discretized by a second-order GFM corrected laplacian scheme, which meets the free surface jump conditions. In addition, the gradient term of the dynamic pressure p_d is also treated with a second-order GFM corrected gradient scheme for the non-orthogonal correction. As for the phase fraction transport equation, it is solved by a PLIC corrected scheme. For pressure–velocity coupling, the PIMPLE algorithm, which is a combination of PISO[32] and SIMPLE,[33] is used to solve it with a segregated strategy. The pressure equation is solved using a preconditioned conjugate gradient (PCG) solver with a diagonal incomplete-Cholesky (DIC) preconditioner, and the tolerance is set to 10^{-8}. Moreover, the phase fraction transport equation is solved by an iterative solver with a symmetric Gauss–Seidel smoother, and the tolerance is set to 10^{-10}.

The simulation is performed on the high performance computing (HPC) cluster of CMHL laboratory at Shanghai Jiao Tong University. Each node consists of 36 CPU cores (2×Intel Xeon Gold 5120, 2.20 GHz) with 128 GB RAM, and three nodes are used for running in parallel. For stability, a fixed time step $\Delta t = 5\times10^{-4}$ s is used throughout the simulation, satisfying the maximum Courant–Friedrichs–Lewy number always less than 0.5. The physical time t is 17 s, and the total CPU running time is about 112 h.

C. Mesh convergence study

A mesh convergence study is first performed on the focused wave generation to determine the appropriate mesh size. The experimental wave parameters used in our study are listed in Table I. Since the wave profiles are the same along the lateral direction, a 2D mesh with only one cell in the y-axis is adopted in this section. The main parameters of three different sets of meshes (namely, coarse, medium, and fine) are presented in Table II.

In our simulations, the number of input wave components is the same as in the experiment, i.e., $N = 244$. Meanwhile, the frequencies are evenly distributed between 0.1 and 2 Hz. Figure 4 compares the wave amplitude spectrum calculated by Eq. (15) with the experimental data. It can be seen that the amplitudes show almost the same distribution, indicating the input parameters are valid.

TABLE I. Experimental wave parameters: x_c, target focus position; T_p, peak wave period; A_c, target crest amplitude; k_p, peak wavenumber; λ_p, peak wavelength; d, water depth; N, total number of wave components.

x_c (m)	T_p (s)	$A_c k_p$	D/λ_p	d (m)	N
4.15	1.456	0.196	0.09	2.93	244

TABLE II. Mesh parameters in 2D convergence study: N_t, total number of cells; Δx, uniform size of refined region in the horizontal direction; Δz, uniform size of refined region in the vertical direction.

Mesh	N_t ($\times10^4$)	Δx (m)	Δz (m)
Coarse	1.8	0.04	0.02
Medium	4.6	0.02	0.01
Fine	6.6	0.01	0.005

Figure 5 compares the time histories of wave elevation η at the focus position. In Fig. 5(a), the wave profiles show a large discrepancy for the coarse mesh, especially in the initial and final phases. Moreover, the crest amplitude is also slightly under-predicted, which can be attributed to the excessive numerical dissipation errors. However, the difference between the medium and fine meshes is minimal, indicating the solution converges with mesh refinement. On this basis, a grid convergence index (GCI) study is carried out on the crest amplitude A_c to quantitatively assess the grid resolution, as shown in Table III. The specific procedures are all under the guidelines of Celik *et al.*[34] Based on the uniform refinement region near the free surface, the grid refinement factor r is a constant equal to 2. The results show that the converge ratio R_G is in the range of 0–1, indicating a monotonic convergence. More importantly, $GCI_{32}/r^P GCI_{21}$ is approximately 1, yielding that the solutions are well within the asymptotic range of convergence. In Fig. 5(b), the result of the medium mesh is further compared with the experimental measurement and the numerical prediction of Hu *et al.*[35] The good agreement with them demonstrates the accuracy of incident wave generation and sufficient mesh configuration. Therefore, the medium mesh is adequate to predict the most common quantities of interest, including wave elevation. Nevertheless, for the main focus of our work, we still employ a 3D mesh (see Fig. 3) of the fine configuration to analyze the near-field of the following wave–structure interaction simulation.

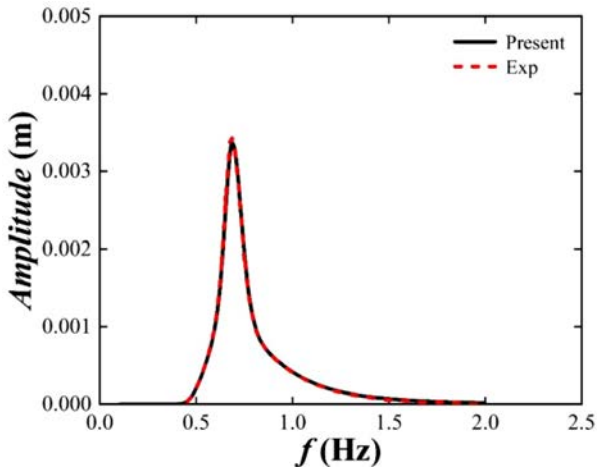

FIG. 4. Comparison of wave amplitude spectra.

Published under an exclusive license by AIP Publishing

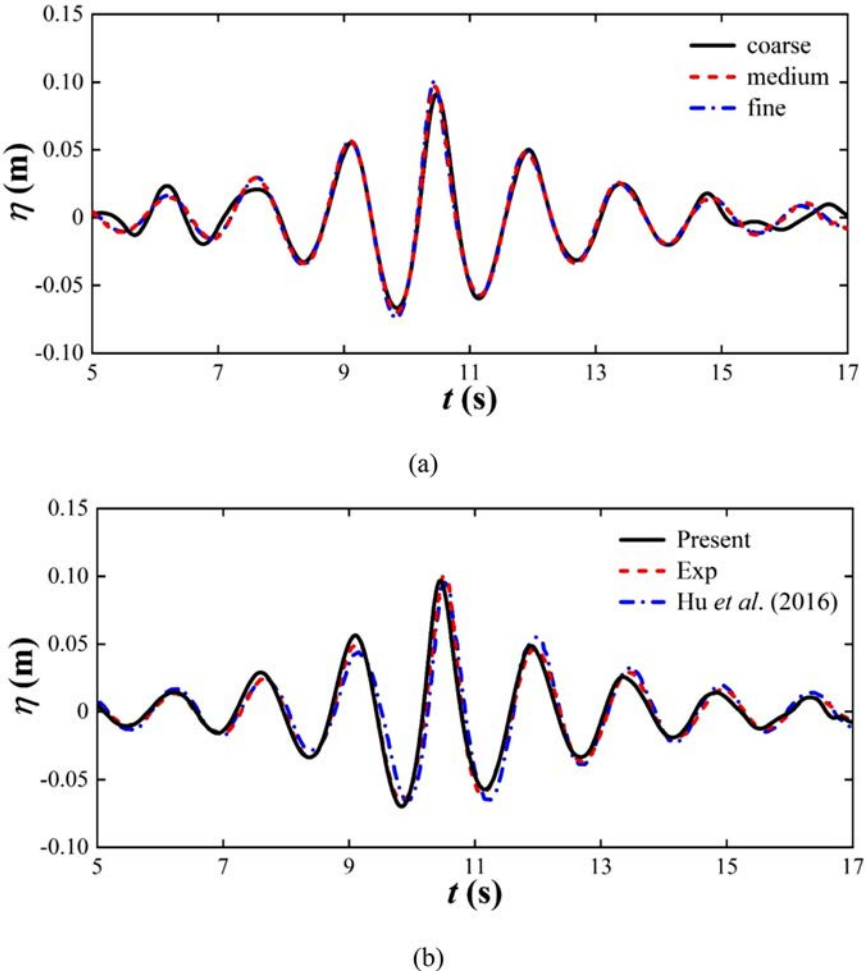

FIG. 5. Time histories of wave elevation at focus position: (a) mesh convergence study and (b) numerical validation.

D. Effects of spurious air velocities

In this section, the effects of spurious air velocities on focused wave generation are discussed, emphasizing the need for the GFM. To intuitively show the difference at first, the comparison of the velocity field at the focus time with/without the GFM is presented in Fig. 6, where the black lines ($\alpha_v = 0.5$) represent the instantaneous free surface. It can be seen from Fig. 6(a) that the velocity field is continuous and smooth across the free surface, and the maximum appears below the wave crest as expected. However, without using the GFM, some spurious velocities (dark red areas) occur above the free surface, as shown in Fig. 6(b). It is worth noting that this problem is particularly evident at the wave crests and troughs. Figure 7 further compares the vorticity field at the focus time with/without the GFM. In Fig. 7(b), the vorticity is much higher above the entire free surface with a more chaotic distribution. However, after using the GFM, it is clearly observed from Fig. 7(a) that the non-zero vorticity is confined to a small region in the vicinity of the free surface, indicating the velocity field is greatly improved. For quantitative statistics, Fig. 8 compares the time histories of wave elevation at the focus position with/without the GFM, where the dashed lines indicate the actual focus time. When the GFM is not used, it gives an earlier focus time and a slightly reduced crest amplitude, which can be attributed to the above observed spurious air velocities.

By comparing various aspects of interest, we conclude that the spurious air velocities can be well eliminated with the GFM, thereby

TABLE III. Grid convergence index (GCI) study for A_c: $\varepsilon_{21} = S_2 - S_1$ and $\varepsilon_{32} = S_3 - S_2$, absolute errors where S denotes the solution of each mesh; r, constant grid refinement factor; $R_G = \varepsilon_{21}/\varepsilon_{32}$, convergence ratio; P, apparent order of convergence; subscripts 1, 2, and 3 represent the fine, medium and coarse meshes, respectively.

Parameter	Value
ε_{21} (m)	−0.003 24
ε_{32} (m)	−0.005 05
r	2
R_G	0.643
P	0.638
GCI_{21} (%)	7.29
GCI_{32} (%)	11.72
$GCI_{32}/r^P GCI_{21}$	1.03

Published under an exclusive license by AIP Publishing

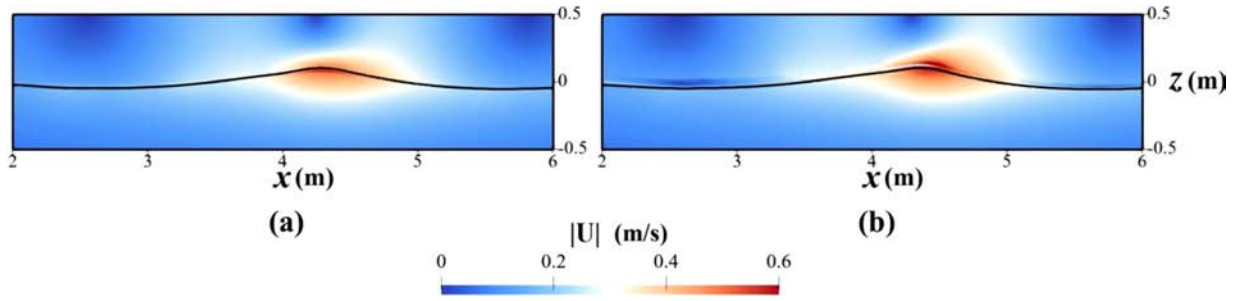

FIG. 6. Velocity fields at focus time: (a) with GFM and (b) without GFM.

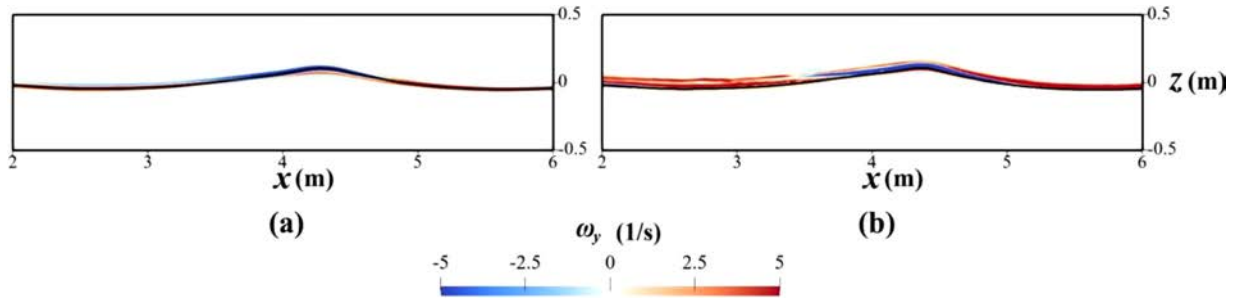

FIG. 7. Vorticity fields at focus time: (a) with GFM and (b) without GFM.

improving the robustness and accuracy of numerical simulations. This improvement guarantees stable wave propagation in steep conditions without any wave breaking caused by large unphysical velocities, which was reported in Ref. 9. On the other hand, because most vortex identification methods are based on the calculation of the velocity field, the more accurate the velocity field, the more accurate the vortical structures, i.e., free from any possible contamination and misleading caused by spurious velocities. This feature is critical for numerical simulations of more complex wave–structure interactions, especially for the in-depth analysis of small-scale free surface flow structures.

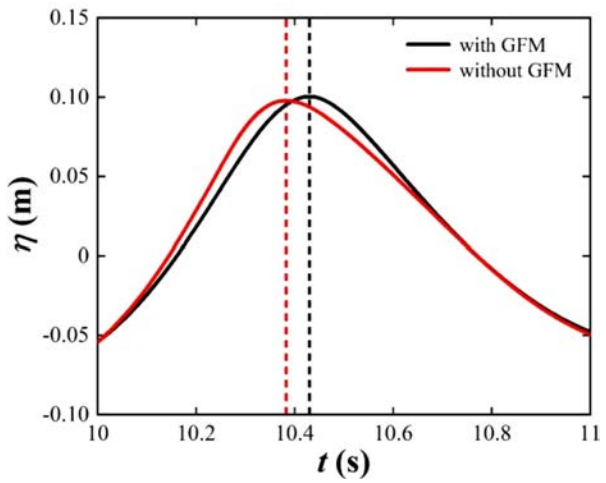

FIG. 8. Time histories of wave elevation at focus position with/without GFM.

IV. RESULTS AND DISCUSSION

A. Comparisons with experiment

Before analyzing the flow field, the results are first quantitatively compared with experimental measurements to validate our numerical model again. Figure 9 shows the locations of wave probes on the cylinder surface, of which WPB1 aims to record the wave run-up height at the front. The other four probes are evenly located on the cylinder surface at an interval of 45°. Figure 10 compares the time histories of wave elevation at WPB1. As can be seen, the present result is in reasonable agreement with the experiment and the numerical simulation of Hu *et al.*[35] However, in our simulation, we find that the maximum

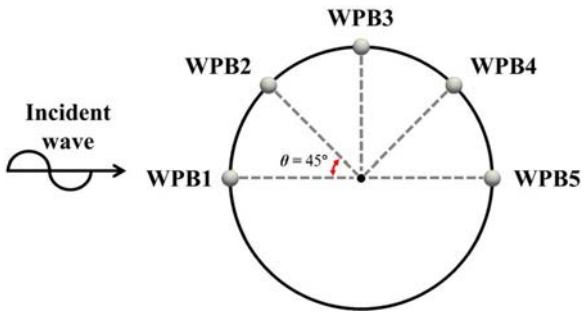

FIG. 9. Locations of wave probes.

Published under an exclusive license by AIP Publishing

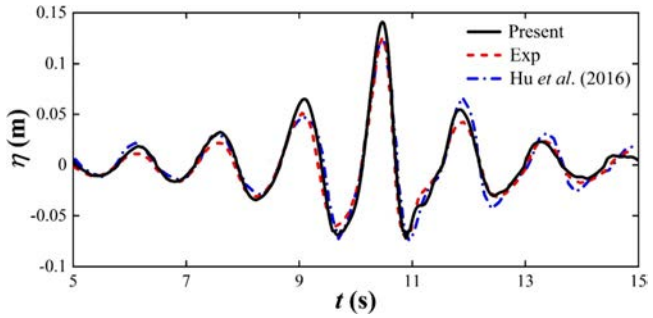

FIG. 10. Time histories of wave elevation at WPB1.

wave run-up is over-predicted. This discrepancy may be due to the virtual wave probes can be infinitely positioned close to the cylinder surface in the numerical simulation.

In the experiment, a pressure sensor was positioned 0.05 m below still water at the front of the cylinder, as illustrated in the enlargement of Fig. 2. In Fig. 11, the comparison of time histories shows that the present numerical model can accurately predict the pressure with a relative error of less than 3% for the peak. On the other hand, when in the significant wave troughs, the pressure drops to zero due to the emergence of the sensor above the free surface. This phenomenon is manifested as straight lines in the time histories, which is also well captured in our simulation.

B. High-frequency wave scattering

Figure 12 shows the time histories of wave elevation at each wave probe. When the focused wave crest comes to the cylinder, a steep wave run-up can be detected at the front stagnation point (WPB1), as shown in Fig. 12(a). The maximum wave elevation can reach about 0.15 m, which is approximately the cylinder's radius. As the wave crest further propagates downstream, a water mound that forms on the back of the cylinder is responsible for a high wave elevation at the rear stagnation point (WPB5). With the crest traveling farther, Fig. 12(b) shows a significant secondary peak (indicated by the red arrow) at WPB3, corresponding to the local disturbance marked by the red dashed circle in Fig. 14(f), which is attributed to the scattered waves near the cylinder surface. Similarly, another small peak occurs at WPB4, as shown in the enlargement. Its earlier occurrence suggests

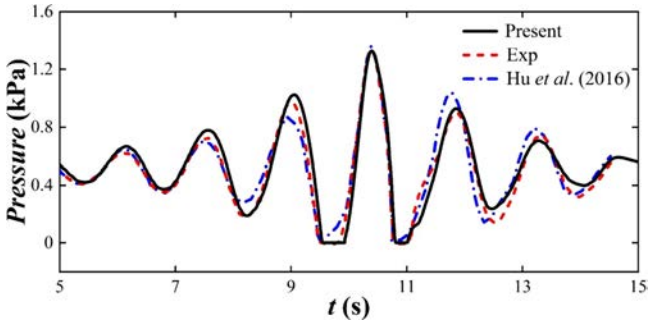

FIG. 11. Time histories of pressure 0.05 m below still water at the front of the cylinder.

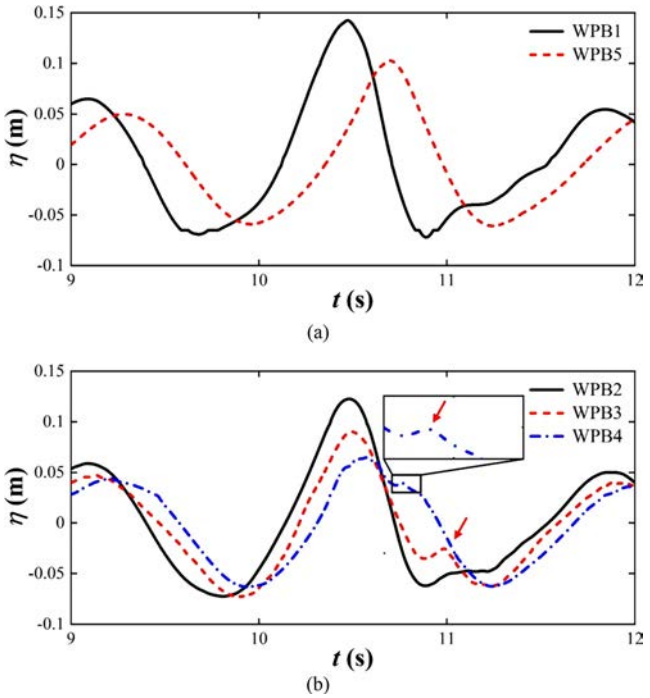

FIG. 12. Time histories of wave elevation at (a) WPB1 and WPB5, and (b) WPB2–WPB4.

that this scattered wave, i.e., the above-mentioned local disturbance on the cylinder surface [see Fig. 14(d)], propagates along the upstream direction and gradually develops in amplitude. However, this secondary peak quickly cannot be detected on the cylinder surface and only appears as a horizontal line at WPB2. The main reason is that this scattered wave gradually radiates outward rather than remaining attached closely to the cylinder surface, which can be well indicated by the evolution of the related vortical structures in Figs. 16(c)–16(e) and 19(g)–19(i).

To intuitively visualize the wave field, Fig. 13 shows the contours of wave elevation at a sequence of time instants. The focused wave propagates from left to right, as indicated by the black arrows in the upper left. When the maximum wave run-up arises at the front stagnation point, the symmetrical scattered waves known as *Type*-2 can be roughly observed at the rear side, as shown in Fig. 13(a). As the *Type*-2 waves further develop downstream along the cylinder surface, they merge at the rear stagnation point to form an apparent water mound [see Figs. 13(b) and 13(c)]. Meanwhile, the concentric scattered wave known as *Type*-1 propagates outward because of the flow induced by the run-up and the subsequent wash-down. When the wave crest passes through the cylinder, the water mound begins to travel back upstream along the cylinder surface, which is responsible for the generation of *Type*-2 wave again. At the same time, the *Type*-1 wave generated in the early phase gradually gets dampened with traveling farther outward, as shown in Fig. 13(d). However, Fig. 13(e) shows that another evident concentric scattered wave known as *Type*-1* wave arises immediately in front of the cylinder, which is consistent with the numerical results by Kasiman.[21] Under the negative velocities induced by the wave trough, the *Type*-1* wave propagates upstream,

Published under an exclusive license by AIP Publishing

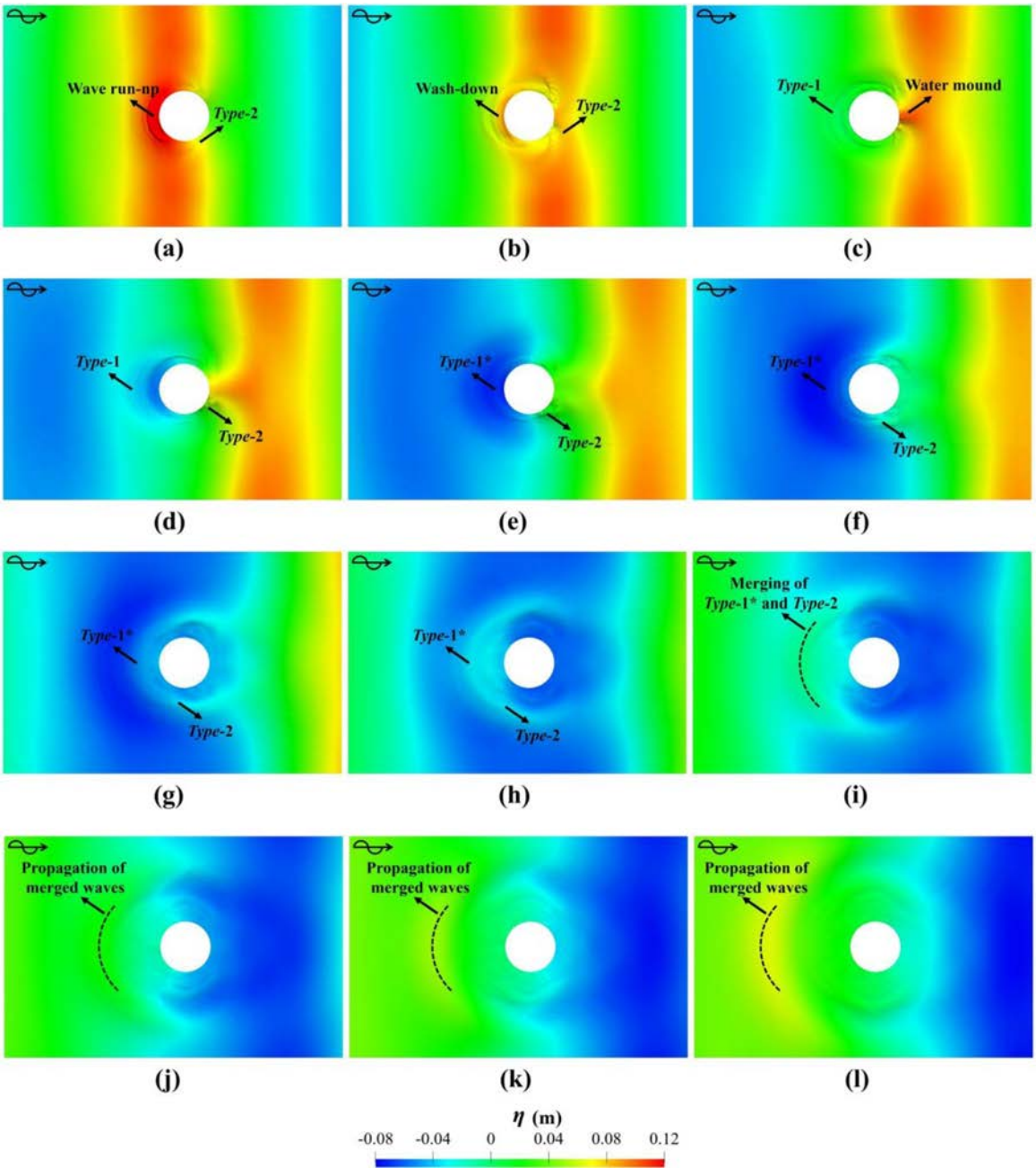

FIG. 13. Contours of wave elevation at (a) $t = 10.46$ s, (b) $t = 10.6$ s, (c) $t = 10.7$ s, (d) $t = 10.8$ s, (e) $t = 10.9$ s, (f) $t = 11$ s, (g) $t = 11.1$ s, (h) $t = 11.2$ s, (i) $t = 11.3$ s, (j) $t = 11.4$ s, (k) $t = 11.5$ s, and (l) $t = 11.6$ s.

opposite to the incident wave direction. At the same time, a pair of symmetrical *Type*-2 waves also travel upstream around the cylinder, one in the clockwise direction and the other in the counterclockwise direction [especially see Fig. 13(g)]. Because of the difference in propagation speed, the *Type*-2 waves gradually catch up with the *Type*-1* wave and finally merge with it into a larger concentric wave, as shown in Figs. 13(h) and 13(i). As the merged wave continues to propagate upstream, it gradually grows steeper in the far field under the interaction with the next incident wave crest.

From the above observations, it is found that the high-frequency wave scattering, especially for the *Type*-2 wave, is strongly related to the flow around the cylinder surface. Therefore, Fig. 14 gives the instantaneous free surface streamlines near the cylinder and the profiles of wave elevation around the cylinder surface at several

Published under an exclusive license by AIP Publishing

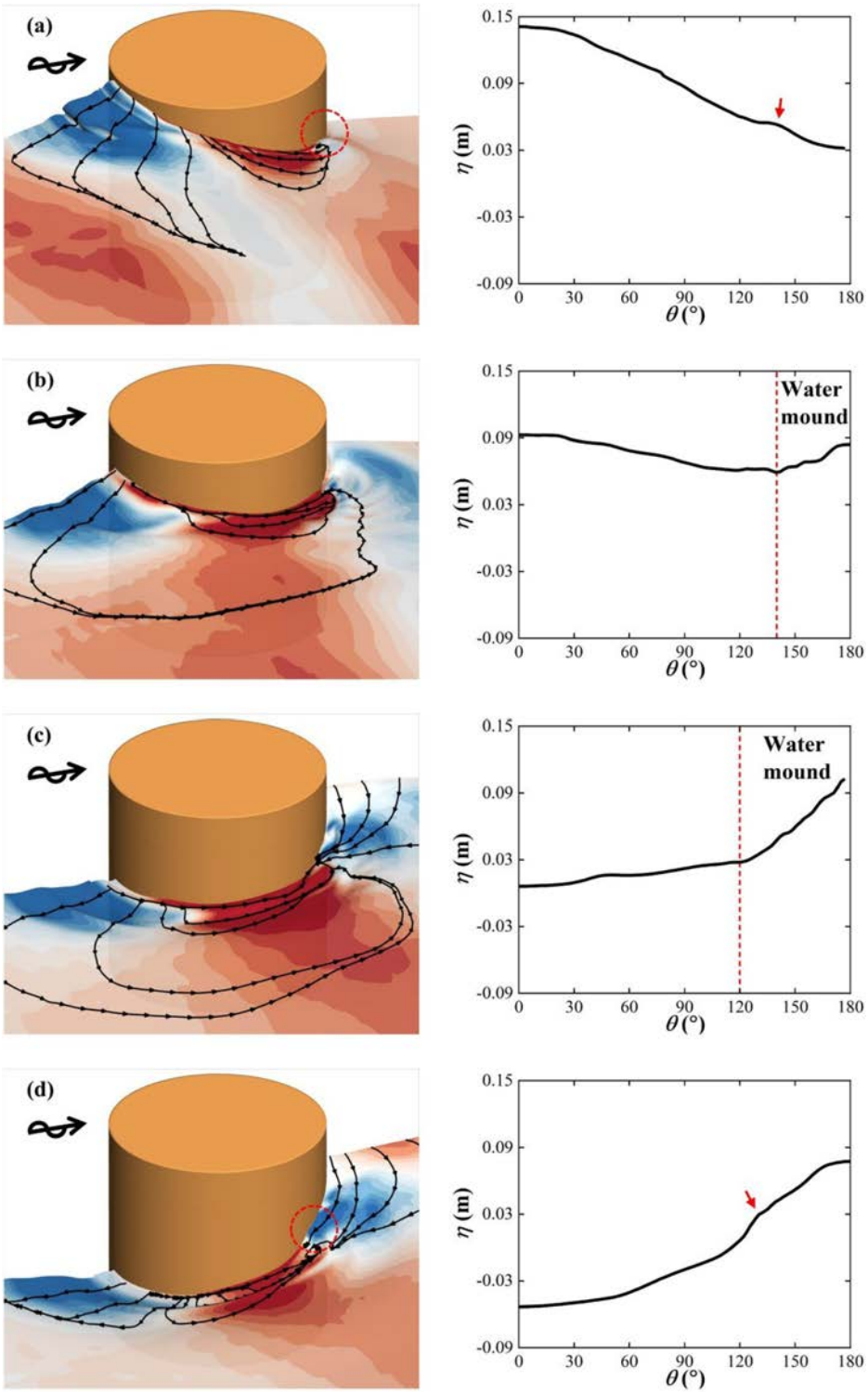

FIG. 14. Flow around cylinder surface at (a) $t = 10.46$ s, (b) $t = 10.6$ s, (c) $t = 10.7$ s, (d) $t = 10.8$ s, (e) $t = 10.9$ s, and (f) $t = 11$ s. (The left columns are the instantaneous free surface streamlines near the cylinder, and the right columns are the profiles of wave elevation around the cylinder surface.)

Published under an exclusive license by AIP Publishing

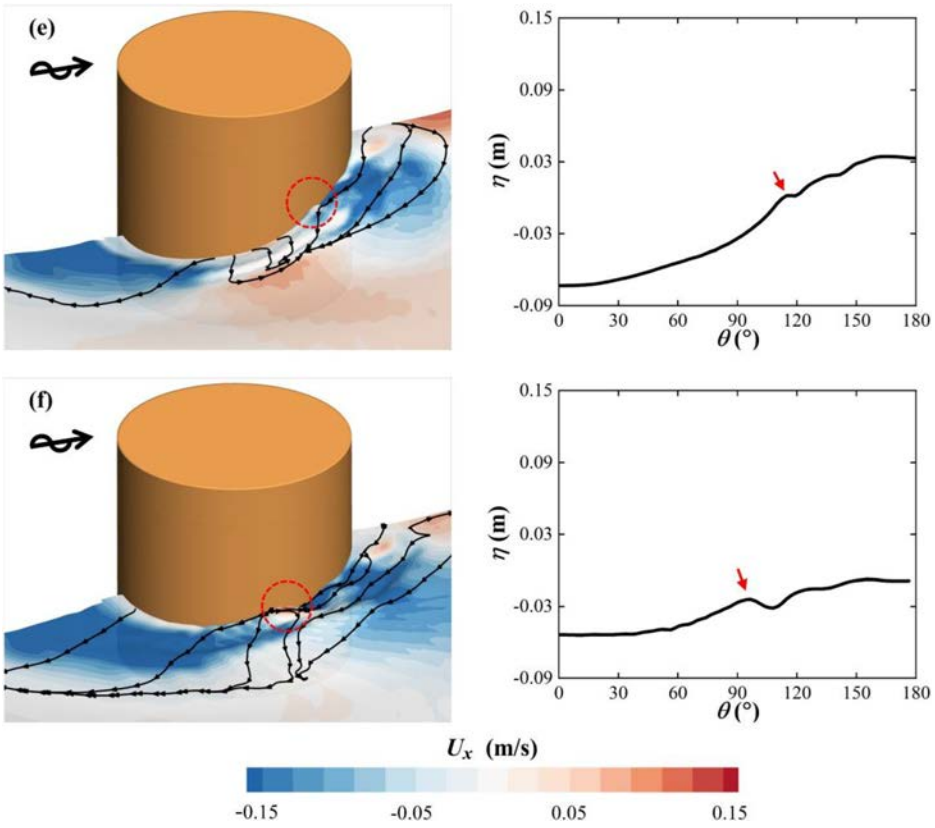

FIG. 14. Flow around cylinder surface at (a) $t = 10.46$ s, (b) $t = 10.6$ s, (c) $t = 10.7$ s, (d) $t = 10.8$ s, (e) $t = 10.9$ s, and (f) $t = 11$ s. (The left columns are the instantaneous free surface streamlines near the cylinder, and the right columns are the profiles of wave elevation around the cylinder surface.)

representative time instants. Due to the symmetry of the flow field, only half of the results are shown for clarity.

In Fig. 14(a), a local disturbance (marked by the red circle) can be seen at the rear of the cylinder surface, which corresponds to a small peak (indicated by the red arrow) in the profile. This disturbance is caused by the movement of fluid along the sides, as suggested by the streamlines and the streamwise velocity contour. When the steep wave crest meets the cylinder, some fluid moves upward and then reverses back at the free surface due to gravity. Meanwhile, as shown by the dark red region near the cylinder, other fluid with high positive velocities moves along the sides. When these disturbances on both sides meet on the back, their superimposition leads to the significant amplification of wave elevation (referred to as the water mound in Fig. 13). This amplification is manifested as a steep slope in the profiles where the red dashed lines represent the beginning, as shown in Figs. 14(b) and 14(c). During this process, the wash-down occurs at the front simultaneously, which leads to the generation of the *Type*-1 wave. With the wave elevation at the back reaching its maximum, a similar wash-down occurs inevitably and creates another small disturbance, as shown in Fig. 14(d). From the perspective of time history, this local disturbance appears as a secondary peak when observed at a fixed position, i.e., the small secondary peak at WPB4 in Fig. 12(b). Under the negative velocities, this disturbance moves in the clockwise direction and interacts with the fluid still moving downstream. As a result, this disturbance grows rapidly and becomes more evident in the profiles, as shown by the red arrow in Fig. 14(f) and the secondary peak at WPB3. With the arrival of the subsequent wave through, the flow field is gradually dominated by the wave-induced negative velocities, and the positive velocities are confined to a shrinking area near the cylinder. The whole development can be clearly seen in Figs. 14(d)–14(f).

C. Vortical structures

In this section, we take a preliminary insight into the vortical structures[36] involved in this complex condition (high fluid velocities induced by the focused wave crest and the existence of the short free end) and attempt to find their relationships with the wave scattering.

The third generation of vortex identification method—Liutex—proposed by Liu *et al.*[37–39] is adopted to represent the vortical structures. This method can extract the pure rigid-body rotation through the decomposition of the fluid motion and obtain the local rotational axis. Compared with other traditional vortex identification methods like Q[40] and λ_2,[41] this unique strength enables it can exclude the possible shearing contamination from a rigorous mathematical perspective. Since the wave motion is essentially a shear flow, the Liutex method is considered the most suitable vortex identification method in wave-structure interaction problems.

The definition of the Liutex vector **R** is given as below:

Published under an exclusive license by AIP Publishing

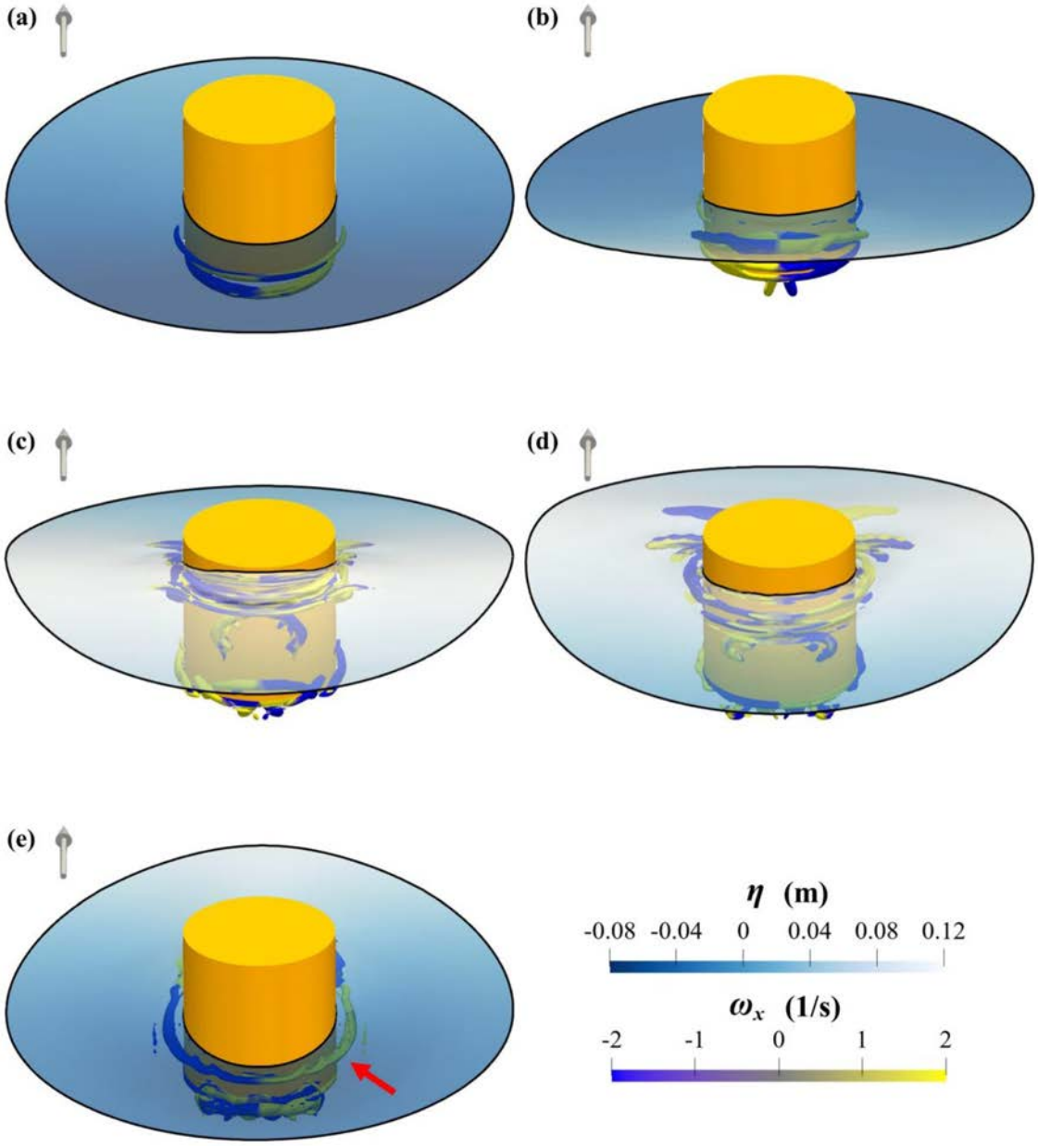

FIG. 15. Instantaneous iso-surfaces of Liutex magnitude $R = 8$ from the front view at (a) $t = 9.68$ s, (b) $t = 10.1$ s, (c) $t = 10.46$ s, (d) $t = 10.6$ s, and (e) $t = 10.9$ s, colored by instantaneous streamwise vorticity.

$$\nabla \mathbf{u} = \mathbf{Q}\nabla\mathbf{U}\mathbf{Q}^T = \begin{bmatrix} \frac{\partial u_x}{\partial x} & \frac{\partial u_x}{\partial y} & 0 \\ \frac{\partial u_y}{\partial x} & \frac{\partial u_y}{\partial y} & 0 \\ \frac{\partial u_z}{\partial x} & \frac{\partial u_z}{\partial y} & \frac{\partial u_z}{\partial z} \end{bmatrix}, \tag{20}$$

where $\mathbf{u}$ is the velocity in the transformed coordinate system, and $\mathbf{Q}$ is the rotational matrix,

$$\mathbf{R} = R\mathbf{r}, \tag{21}$$

$$R = \begin{cases} 2(B - A), & A^2 - B^2 < 0 \quad \text{and} \quad B > 0, \\ 2(B + A), & A^2 - B^2 < 0 \quad \text{and} \quad B < 0, \\ 0, \end{cases} \tag{22}$$

$$\begin{cases} A = \frac{1}{2}\sqrt{\left(\frac{\partial u_y}{\partial y} - \frac{\partial u_x}{\partial x}\right)^2 + \left(\frac{\partial u_y}{\partial x} + \frac{\partial u_x}{\partial y}\right)^2}, \\ B = \frac{1}{2}\left(\frac{\partial u_y}{\partial x} - \frac{\partial u_x}{\partial y}\right), \end{cases} \tag{23}$$

Published under an exclusive license by AIP Publishing

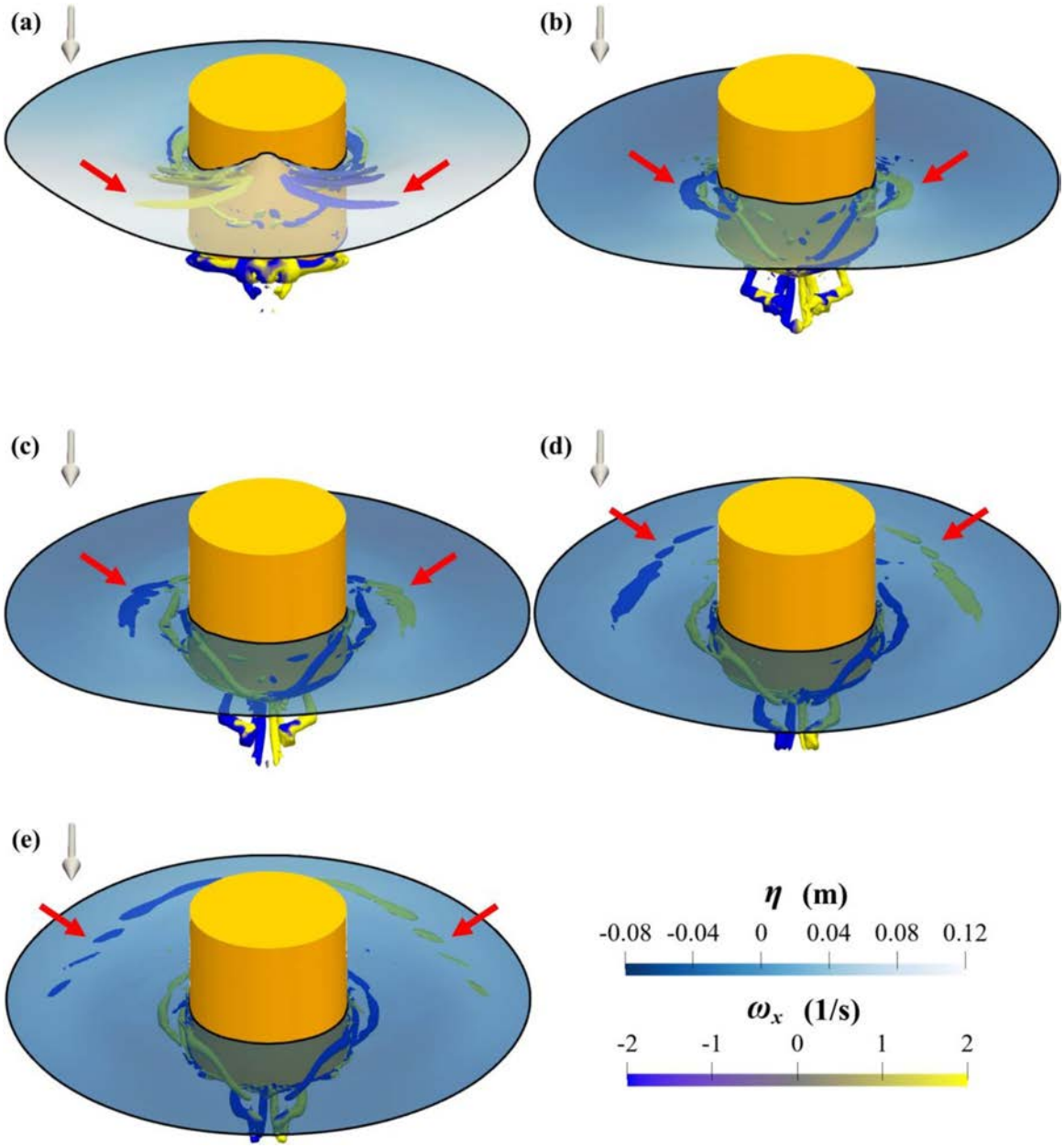

FIG. 16. Instantaneous iso-surfaces of Liutex magnitude $R = 8$ from the back view at (a) $t = 10.7$ s, (b) $t = 11$ s, (c) $t = 11.1$ s, (d) $t = 11.2$ s, and (e) $t = 11.3$ s, colored by instantaneous streamwise vorticity.

where R is the magnitude of the Liutex vector, and $\mathbf{r}$ is the real eigenvector of the velocity gradient $\nabla\mathbf{u}$, i.e., local rotational direction.

Figure 15 shows the development of instantaneous vortical structures during the wave run-up from the front view. The iso-surfaces of Liutex magnitude $R = 8$ represent the vortical structures in the water phase, and the transparent free surfaces are also given to determine their relative positions. When the previous large-amplitude wave trough passes through the cylinder, the wave-induced high negative velocities generate some vortical structures near the free end, as shown in Fig. 15(a). These structures are complete and mainly surround the front cylinder surface. With the arrival of the following focused crest, they gradually move upward and approach the free surface. Their interaction with the free surface is one of the reasons for such small-scale vortical structures below the maximum wave elevation, as shown in Fig. 15(c). Another important reason is the roll-up of local fluid caused by the steep wave run-up on the front surface visualized later.

Published under an exclusive license by AIP Publishing

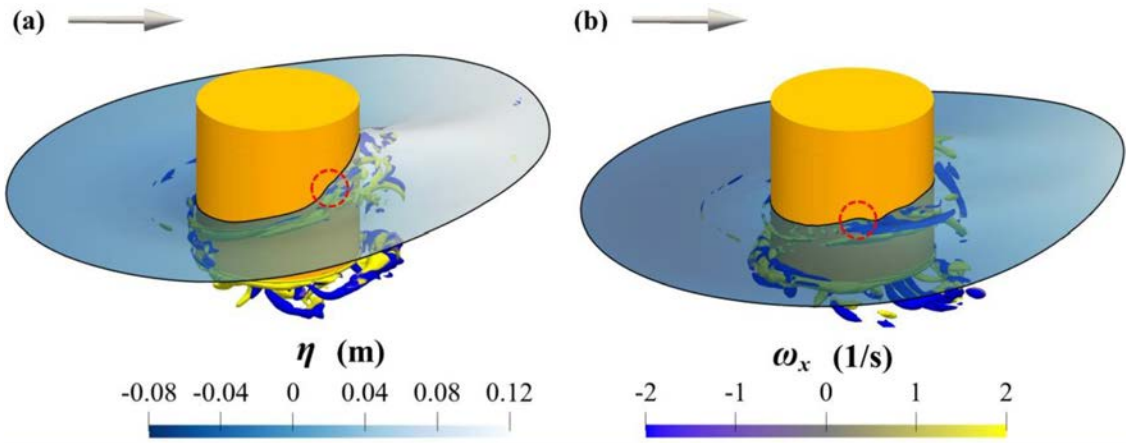

FIG. 17. Instantaneous iso-surfaces of Liutex magnitude $R = 8$ from the side view at (a) $t = 10.8$ s and (b) $t = 11$ s, colored by instantaneous streamwise vorticity.

Then, as the wash-down occurs, these small-scale structures propagate outward in a concentric pattern, which is very similar to the *Type*-1 wave [see Fig. 15(d)]. More notably, when these vortical structures gradually dissipate and propagate to the far field, Fig. 15(e) shows another apparent structure (indicated by the red arrow) surrounding the cylinder in the front. The occurrence of this specific structure exactly corresponds to the onset of the *Type*-1* wave observed in Fig. 13(e).

Moreover, Fig. 16 shows the development of instantaneous vortical structures during the wash-down of the water mound from the back view. When the water mound is formed on the back, a pair of counter-rotating vortices (indicated by red arrows) can be identified below the free surface in Fig. 16(a). As the fluid of the water mound travels back, they create local disturbances on both sides near the cylinder surface, as already discussed in Fig. 14. After the rapid growth of these disturbances, another pair of counter-rotating vortices can be seen below the *Type*-2 waves in Figs. 16(b) and 16(c). Under the negative velocities induced by the wave trough, the symmetrical vortices move upstream and gradually radiate away from the cylinder surface, which could explain why no secondary peak is detected at WPB2.

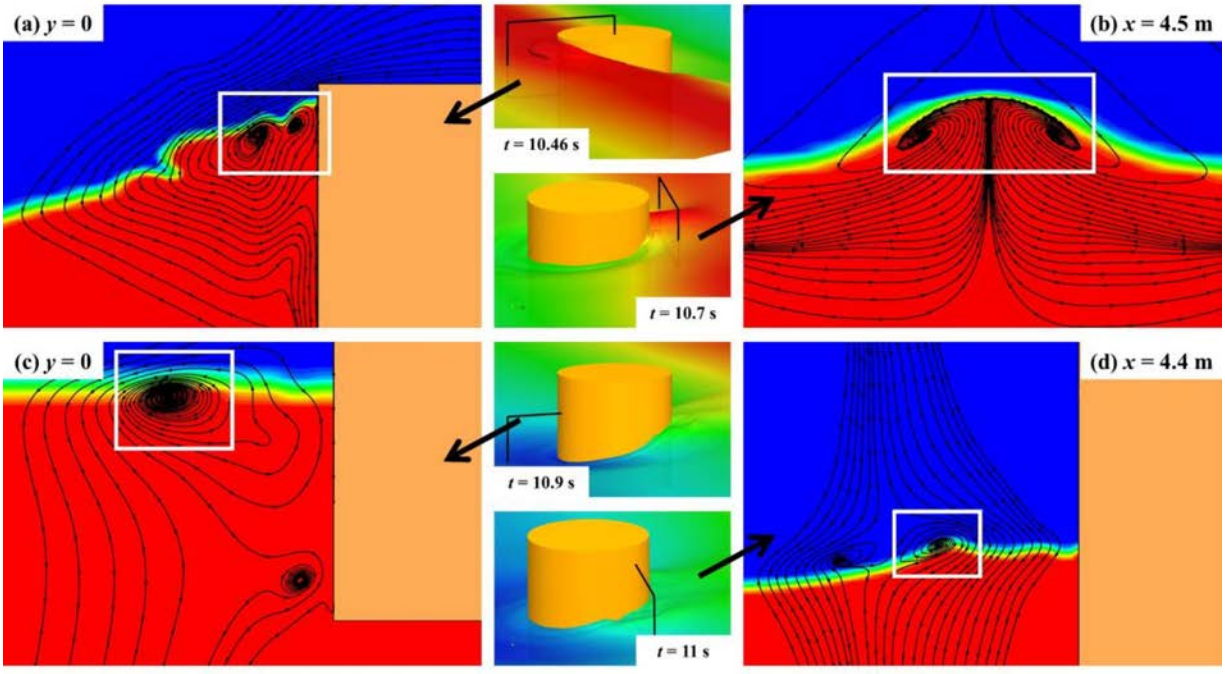

FIG. 18. Instantaneous streamlines on specific planes, colored by phase fraction.

Published under an exclusive license by AIP Publishing

This behavior is generally consistent with the experimental observation of Swan and Sheikh.[3] More importantly, the development of these vortical structures further confirms the tail of the above disturbances moves in a spiral fashion, which cannot be recognized easily from the free surface in previous studies. When the vortices move further upstream, they merge into a semicircle and continue to spread outward, as shown in Figs. 16(d)–16(e). It can be seen from the incomplete structure that its magnitude is decreasing, indicating the scattered waves get dampened in the far field.

Figure 17 shows a side view of vortical structures to reveal their relationship to the local disturbance on the cylinder surface (marked by red dashed circles). Two representative time instants are chosen here, which in turn correspond to the occurrence of the secondary peak in Fig. 12(b). As shown in Fig. 17(a), the apparent counter-rotating

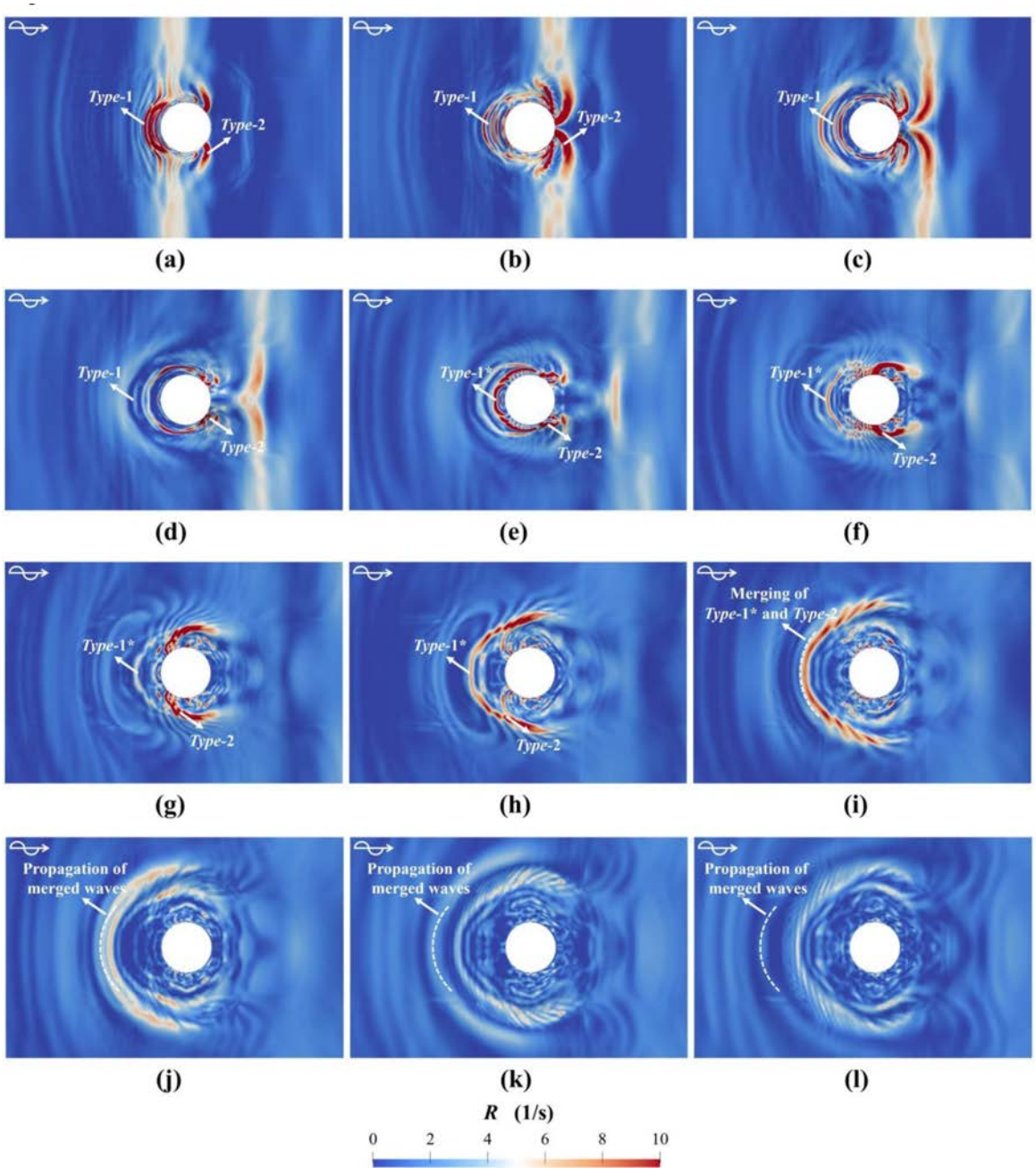

FIG. 19. Contours of Liutex magnitude R at (a) $t = 10.46$ s, (b) $t = 10.6$ s, (c) $t = 10.7$ s, (d) $t = 10.8$ s, (e) $t = 10.9$ s, (f) $t = 11$ s, (g) $t = 11.1$ s, (h) $t = 11.2$ s, (i) $t = 11.3$ s, (j) $t = 11.4$ s, (k) $t = 11.5$ s, and (l) $t = 11.6$ s.

Published under an exclusive license by AIP Publishing

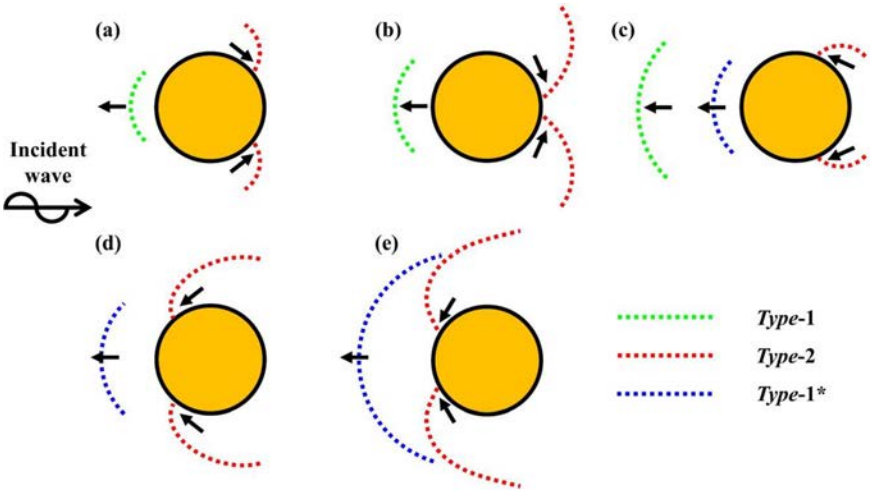

FIG. 20. Schematic of wave scattering evolution during one wave crest period: (a) stage I, (b) stage II, (c) stage III, (d) stage IV, and (e) stage V.

vortices are not generated immediately when the local disturbance is initialized at the early stage. Instead, many small-scale vortices gather below the free surface, indicating the nearby flow is very unstable at this time. As this disturbance develops upstream along the cylinder surface, the dominant counter-rotating vortices can be captured, with their head just below the disturbance. This feature shows that the counter-rotating vortices develop synchronously with the local disturbance, confirming their strong correlations.

To more intuitively show the local fluid motion below the scattered waves, the instantaneous streamlines on several specific planes are displayed in Fig. 18. The planes are colored by the phase fraction to represent the free surface. In Fig. 18(a), some fluid is obstructed by the cylinder and forced to move upward along the front surface. During the reverse flow due to gravity, it rolls up into two small vortices below the free surface. This flow behavior can vividly explain the formation of the *Type*-1 wave in the steep wave conditions. In Fig. 18(b), the flows from both sides converge on the centerline and then move upward, forming the apparent water mound. Similarly, the flows spread outward again on the free surface and roll up into a pair of counter-rotating vortices corresponding to the vortical structures in Fig. 16(a). In Fig. 18(c), it can be seen that a large vortex is below the *Type*-1* wave when the wave elevation reaches the lowest at the front stagnation point (WPB1). At this time, the sustained wash-down on the front surface just ends. Most of the gravitational potential energy accumulated during the steep run-up is converted into kinetic energy. As a result, the wave elevation is much lower than the incident condition without the presence of the cylinder. After that, the subsequent significant increase in wave elevation induces a rapid upward movement of the fluid near the cylinder surface, which is termed "bounce-back" by Kasiman.[21] This phenomenon is responsible for the generation of this large vortex. In Fig. 18(d), the streamlines on a transverse plane further reveal the detailed behavior of the *Type*-2 wave. In the contour of phase fraction, the *Type*-2 wave is manifested as a slight rise on the free surface. Below it, a small vortex can be seen corresponding to the structures in Fig. 16(b) with another induced one in the air phase. The visualization of this vortex further confirms the outward spiral motion of the *Type*-2 wave.

From the above analysis, it is evident that the high-frequency scattered waves are associated with several primary vortical structures. In other words, these vortical structures appear as high-frequency scattered waves on the free surface. Furthermore, the behaviors of these vortical structures could reveal the evolution of scattered waves. On this basis, we attempt to use the contours of Liutex magnitude on the free surface to identify the high-frequency scattered waves again. As shown in Fig. 19, the high-magnitude regions colored in red well depict the patterns of scattered waves. Compared with other straightforward identification methods, such as surface elevation, this post-processing method is not only more effective in visualization but also provides more details. For example, Figs. 19(a) and 19(b) clearly show the generation of the *Type*-1 wave during the run-up and wash-down. Its subsequent dissipation in the far field can also be seen from the gradually decreasing magnitude. In addition, Fig. 19(d) further confirms that the initial disturbances of the *Type*-2 wave originate from the cylinder surface, which is not evident in the wave profiles. What is more, Figs. 19(g)–19(j) illustrate the evolution of the merging of *Type*-1* and *Type*-2 waves from a more intuitive perspective. According to their patterns and magnitudes, an overall schematic of wave scattering evolution in the present condition is summarized in Fig. 20.

V. CONCLUSIONS

In this paper, the wave scattering of the focused wave by a finite surface-piercing circular cylinder is numerically investigated. The GFM is implemented to eliminate the spurious air velocities, and the GABC boundary conditions are adopted for wave generation and absorption with high computational efficiency. The established high-fidelity numerical wave tank is proven to be accurate and reliable by comparison with experimental measurements in 2D wave propagation and 3D wave–structure interaction. On this basis, the high-frequency scattered waves involved in this complex condition are identified and analyzed, providing new insights into wave scattering. The main conclusions are as follows:

1. The current implementation of the GFM works well to eliminate the spurious air velocities above the free surface in focused wave simulations, achieving a more physical flow field. By contrast, the spurious air velocities result in an earlier focus time and a slightly reduced crest amplitude.

Published under an exclusive license by AIP Publishing

2. Visualization of the flow field reveals the mechanisms of three types of high-frequency scattered waves, which are *Type*-1, *Type*-2, and *Type*-1*, respectively. The concentric *Type*-1 wave is attributed to the run-up and wash-down after encountering the focused crest. The symmetrical *Type*-2 waves are highly associated with the flow around the cylinder and first initialize as disturbances on the cylinder surface. The bounce-back after the sustained wash-down at the front, which only appears in focused waves, is responsible for the concentric *Type*-1* wave.
3. Primary vortical structures are extracted below the high-frequency scattered waves using the Liutex vortex identification method. Semicircular structures surrounding the front cylinder surface correspond to the concentric *Type*-1 and *Type*-1* waves, and a pair of counter-rotating slender structures correspond to the symmetrical *Type*-2 waves. Their behaviors could characterize the evolution of scattered waves and reveal more details, such as spiral motions of tails.
4. Based on the above identifications and analysis, an overall schematic of wave scattering evolution in the focused wave interactions with a finite surface-piercing circular cylinder is summarized. It could well complement previous studies on regular waves and gain a straightforward understanding of this highly nonlinear phenomenon.

In the future, we will perform a systematical parametric study and focus on studying the variation of these high-frequency scattered waves and the correlated vortical structures with various factors of interest, including wave steepness (kA) and cylinder diameter (D).

ACKNOWLEDGMENTS

This work is supported by the National Natural Science Foundation of China (Grant Nos. 51879159, 52131102, and 51909160), and the National Key Research and Development Program of China (Grant No. 2019YFB1704200), to which the authors are most grateful.

AUTHOR DECLARATIONS

Conflict of Interest

The authors have no conflicts of interest to disclose.

DATA AVAILABILITY

The data that support the findings of this study are available from the corresponding author upon reasonable request.

APPENDIX: NUMERICAL IMPROVEMENTS BY THE GFM

In this appendix, we demonstrate the significant numerical improvements by the GFM using a standard test case for free surface flows, which is also adopted for validation in Refs. 14 and 15. Figure 21 illustrates a 2D computation domain, where the interface between two inviscid fluids is the initial position. It is worth noting that the 1:1000 density ratio between these two fluids can well represent the air–water two-phase flows in this study. When the uniform flow with velocity **U** enters from the inlet, the free surface at the outlet will gradually rise due to the ramp and finally reach a steady state. A structured computational mesh that consists of 120×96 cells is used in our simulations. Detailed description and numerical setup can be found in Refs. 14 and 42.

Figures 22–25 compare the flow field from various aspects when the flow reaches a steady state. The improvements with the GFM are on the left, and the original results without the GFM are on the right. For the free surface profile, there is no significant difference from each other, as shown in Fig. 22. However, for the dynamic pressure, a sharp interface between two fluids is well preserved in Fig. 23(a), indicating the free surface jump condition is

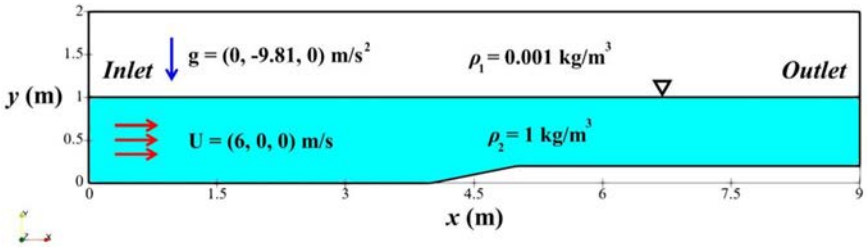

FIG. 21. 2D inviscid free surface flow over a ramp.

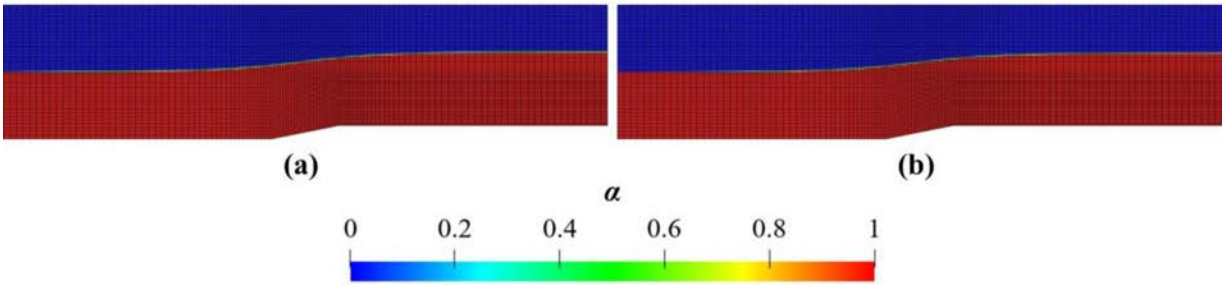

FIG. 22. Comparison of the phase fraction: (a) with GFM and (b) without GFM.

Published under an exclusive license by AIP Publishing

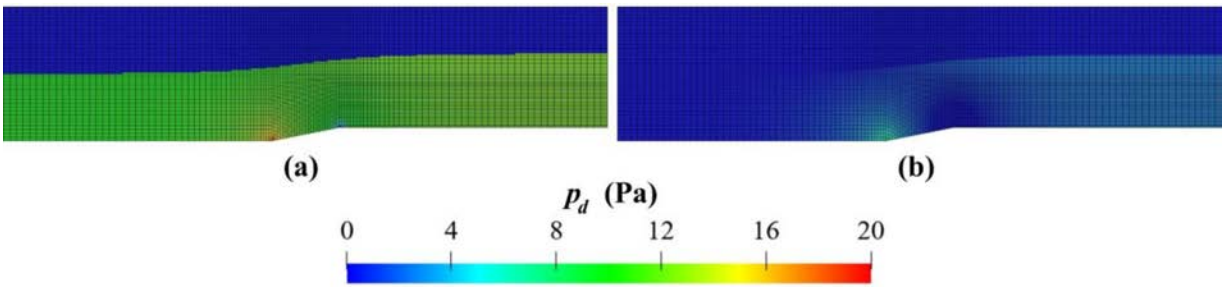

FIG. 23. Comparison of the dynamic pressure: (a) with GFM and (b) without GFM.

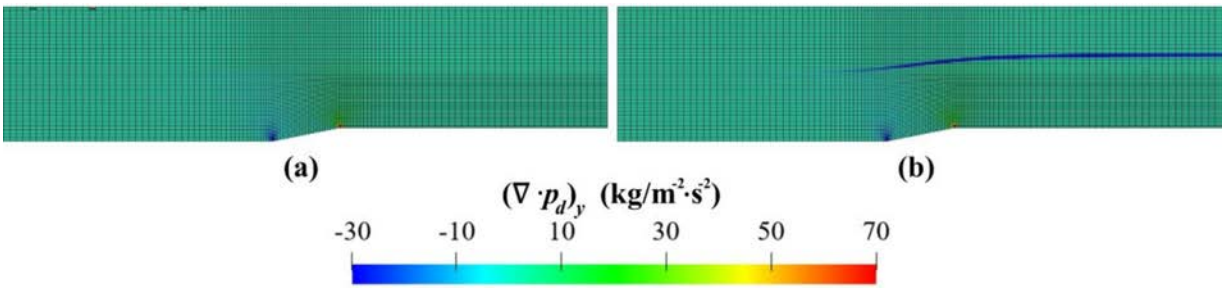

FIG. 24. Comparison of the vertical dynamic pressure gradient: (a) with GFM and (b) without GFM.

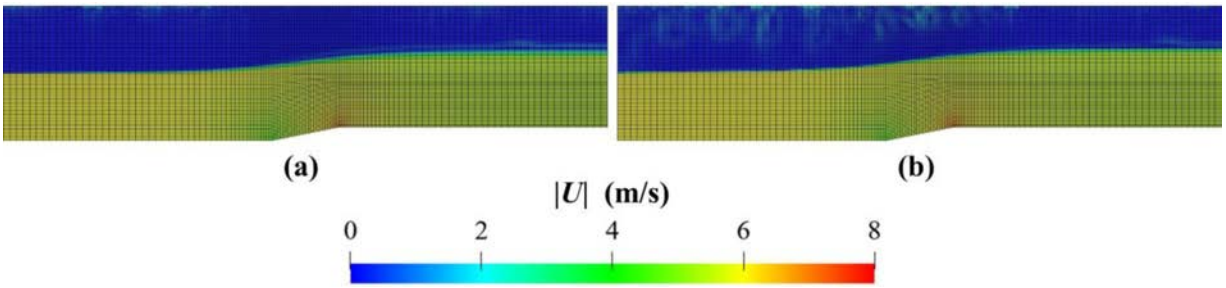

FIG. 25. Comparison of the velocity magnitude: (a) with GFM and (b) without GFM.

achieved with the GFM. The qualitatively similar results can also be found in Ref. 18. For future wave impact problems, this feature is thought to improve the accuracy of predicting peak pressure values. Further post-processing reveals that the vertical pressure gradient is continuous using the above-mentioned one-sided extrapolation. On the contrary, Fig. 24(b) shows that the usual linear interpolation results in an obvious discontinuity in the vicinity of the free surface, which is one of the main reasons for the spurious velocities. For the velocity, Fig. 25(a) shows that the spurious velocities are well eliminated above the free surface, leading to a more stable and continuous field.

REFERENCES

[1]R. Sheikh and C. Swan, "The interaction between steep waves and a vertical, surface-piercing column," J. Offshore Mech. Arct. Eng. **127**, 31–38 (2005).
[2]C. Swan, S. Masterton, R. Sheikh, and A. Cavalletti, "Wave forcing and wave scattering from a vertical surface-piercing cylinder," in *Proceedings of the International Conference on Offshore Mechanics and Arctic Engineering* (ASME, 2005), pp. 571–580.
[3]C. Swan and R. Sheikh, "The interaction between steep waves and a surface-piercing column," Philos. Trans. R. Soc. A **373**, 20140114 (2015).
[4]Z. Fang, L. Xiao, H. Wei, M. Liu, and Y. Guo, "Severe wave run-ups on fixed surface-piercing square column under focused waves," Phys. Fluids **32**, 063308 (2020).
[5]P.-N. Sun, M. Luo, D. L. Touzé, and A.-M. Zhang, "The suction effect during freak wave slamming on a fixed platform deck: Smoothed particle hydrodynamics simulation and experimental study," Phys. Fluids **31**, 117108 (2019).
[6]L. F. Chen, J. Zang, A. J. Hillis, G. C. Morgan, and A. R. Plummer, "Numerical investigation of wave–structure interaction using OpenFOAM," Ocean Eng. **88**, 91–109 (2014).
[7]Q. Chen, J. Zang, D. M. Kelly, and A. S. Dimakopoulos, "A 3D parallel particle-in-cell solver for wave interaction with vertical cylinders," Ocean Eng. **147**, 165–180 (2018).
[8]M. Mohseni, P. T. Esperanca, and S. H. Sphaier, "Numerical study of wave run-up on a fixed and vertical surface-piercing cylinder subjected to regular, non-breaking waves using OpenFOAM," Appl. Ocean Res. **79**, 228–252 (2018).

Published under an exclusive license by AIP Publishing

[9]M. A. Afshar, "Numerical wave generation in OpenFOAM®," Master of Science thesis (Chalmers University of Technology, 2010).
[10]R. P. Fedkiw, T. Aslam, B. Merriman, and S. Osher, "A non-oscillatory Eulerian approach to interfaces in multimaterial flows (the ghost fluid method)," J. Comput. Phys. **152**, 457–492 (1999).
[11]M. Kang, R. P. Fedkiw, and X.-D. Liu, "A boundary condition capturing method for multiphase incompressible flow," J. Sci. Comput. **15**, 323–360 (2000).
[12]J. Huang, P. M. Carrica, and F. Stern, "Coupled ghost fluid/two-phase level set method for curvilinear body-fitted grids," Int. J. Numer. Methods Fluids **55**, 867–897 (2007).
[13]P. Queutey and M. Visonneau, "An interface capturing method for free-surface hydrodynamic flows," Comput. Fluids **36**, 1481–1510 (2007).
[14]V. Vukčević, H. Jasak, and I. Gatin, "Implementation of the ghost fluid method for free surface flows in polyhedral finite volume framework," Comput. Fluids **153**, 1–19 (2017).
[15]P. Peltonen, P. Kanninen, E. Laurila, and V. Vuorinen, "The ghost fluid method for OpenFOAM: A comparative study in marine context," Ocean Eng. **216**, 108007 (2020).
[16]P. Peltonen, P. Kanninen, E. Laurila, and V. Vuorinen, "Scaling effects on the free surface backward facing step flow," Phys. Fluids **33**, 042106 (2021).
[17]V. Vukčević, H. Jasak, and Š. Malenica, "Decomposition model for naval hydrodynamic applications. II. Verification and validation," Ocean Eng. **121**, 76–88 (2016).
[18]V. Vukčević, "Numerical modelling of coupled potential and viscous flow for marine applications," Ph.D. thesis (University of Zagreb, Faculty of Mechanical Engineering and Naval Architecture, 2016).
[19]Z. Li, "Two-phase spectral wave explicit Navier-Stokes equations method for wave-structure interactions," Ph.D. thesis (École centrale de Nantes, 2018).
[20]S. Liu, M. C. Ong, C. Obhrai, I. Gatin, and V. Vukčević, "Influences of free surface jump conditions and different k-ω SST turbulence models on breaking wave modelling," Ocean Eng. **217**, 107746 (2020).
[21]E. H. Kasiman, "Numerical modelling of wave interactions with a vertical surface-piercing column," Ph.D. thesis (Imperial College London, 2017).
[22]H. Rusche, "Computational fluid dynamics of dispersed two-phase flows at high phase fractions," Ph.D. thesis (Imperial College London, University of London, 2003).
[23]H. G. Weller, "A new approach to VOF-based interface capturing methods for incompressible and compressible flow," Report No. TR/HGW4 (OpenCFD Ltd., 2008).
[24]S. Chen, W. Zhao, and D. Wan, "Turbulent structures and characteristics of flows past a vertical surface-piercing finite circular cylinder," Phys. Fluids **34**, 015115 (2022).
[25]N. G. Jacobsen, D. R. Fuhrman, and J. Fredsøe, "A wave generation toolbox for the open-source CFD library: OpenFoam®," Int. J. Numer. Methods Fluids **70**, 1073–1088 (2012).
[26]P. Wellens and M. Borsboom, "A generating and absorbing boundary condition for dispersive waves in detailed simulations of free-surface flow interaction with marine structures," Comput. Fluids **200**, 104387 (2020).
[27]M. Borsboom and N. G. Jacobsen, "A generating-absorbing boundary condition for dispersive waves," Int. J. Numer. Methods Fluids **93**, 2443–2467 (2021).
[28]P. S. Tromans, A. R. Anaturk, and P. Hagemeijer, "A new model for the kinematics of large ocean waves-application as a design wave," in *Proceedings of the First International Offshore and Polar Engineering Conference* (OnePetro, 1991), pp. 64–71.
[29]Y. Goda, "Statistical variability of sea state parameters as a function of wave spectrum," Coastal Eng. Jpn. **31**, 39–52 (1988).
[30]Y. Zhuang and D. Wan, "Parametric study of a new HOS-CFD coupling method," J. Hydrodyn. **33**, 43–54 (2021).
[31]B. E. Larsen, D. R. Fuhrman, and J. Roenby, "Performance of interFoam on the simulation of progressive waves," Coastal Eng. J. **61**, 380–400 (2019).
[32]R. I. Issa, "Solution of the implicitly discretised fluid flow equations by operator-splitting," J. Comput. Phys. **62**, 40–65 (1986).
[33]L. S. Caretto, A. D. Gosman, S. V. Patankar, and D. B. Spalding, "Two calculation procedures for steady, three-dimensional flows with recirculation," in *Proceedings of the Third International Conference on Numerical Methods in Fluid Mechanics* (Springer, 1973), pp. 60–68.
[34]I. B. Celik, U. Ghia, P. J. Roache, and C. J. Freitas, "Procedure for estimation and reporting of uncertainty due to discretization in CFD applications," J. Fluids Eng. **130**, 078001 (2008).
[35]Z. Z. Hu, D. Greaves, and A. Raby, "Numerical wave tank study of extreme waves and wave-structure interaction using OpenFoam®," Ocean Eng. **126**, 329–342 (2016).
[36]G. Antolloni, A. Jensen, J. Grue, B. H. Riise, and M. Brocchini, "Wave-induced vortex generation around a slender vertical cylinder," Phys. Fluids **32**, 042105 (2020).
[37]Y. Gao and C. Liu, "Rortex and comparison with eigenvalue-based vortex identification criteria," Phys. Fluids **30**, 085107 (2018).
[38]C. Liu, Y. Gao, S. Tian, and X. Dong, "RortexĐA new vortex vector definition and vorticity tensor and vector decompositions," Phys. Fluids **30**, 035103 (2018).
[39]Y. Gao and C. Liu, "Rortex based velocity gradient tensor decomposition," Phys. Fluids **31**, 011704 (2019).
[40]J. C. R. Hunt, A. Wray, and P. Moin, "Eddies, stream, and convergence zones in turbulent flows," in *Proceedings of the Summer Program* (Center for Turbulence Research, 1988), pp. 193–208.
[41]J. Jeong and F. Hussain, "On the identification of a vortex," J. Fluid Mech. **285**, 69–94 (1995).
[42]S. Muzaferija and M. Peric, "Computation of free-surface flows using the finite-volume method and moving grids," Numer. Heat Transfer **32**, 369–384 (1997).

Published under an exclusive license by AIP Publishing